NAVAL POSTGRADUATE SCHOOL
Monterey, California

THESIS

SIMULATIONS OF THE PROPOSED TJNAF 100KW FREE ELECTRON LASER AND COMPARISON WITH TJNAF LOW POWER EXPERIMENTS

by

Konstantinos Polykandriotis

December 2001

Thesis Advisor: William B. Colson
Co-Advisor: Robert L. Armstead

Report Documentation Page

Report Date	Report Type	Dates Covered (from... to)
19 Dec 2001	N/A	-

Title and Subtitle Simulations of the Proposed TJNAF 100KW Free Electron Laser and Comparison with TJNAF Low Power Experiments	**Contract Number**
	Grant Number
	Program Element Number
Author(s) Polykandriotis, Konstantinos	**Project Number**
	Task Number
	Work Unit Number
Performing Organization Name(s) and Address(es) Naval Postgraduate School Monterey, California	**Performing Organization Report Number**
Sponsoring/Monitoring Agency Name(s) and Address(es)	**Sponsor/Monitor's Acronym(s)**
	Sponsor/Monitor's Report Number(s)
Distribution/Availability Statement Approved for public release, distribution unlimited	
Supplementary Notes The original document contains color images.	
Abstract	
Subject Terms	
Report Classification unclassified	**Classification of this page** unclassified
Classification of Abstract unclassified	**Limitation of Abstract** UU
Number of Pages 101	

THIS PAGE INTENTIONALLY LEFT BLANK

REPORT DOCUMENTATION PAGE			Form Approved OMB No. 0704-0188
Public reporting burden for this collection of information is estimated to average 1 hour per response, including the time for reviewing instruction, searching existing data sources, gathering and maintaining the data needed, and completing and reviewing the collection of information. Send comments regarding this burden estimate or any other aspect of this collection of information, including suggestions for reducing this burden, to Washington headquarters Services, Directorate for Information Operations and Reports, 1215 Jefferson Davis Highway, Suite 1204, Arlington, VA 22202-4302, and to the Office of Management and Budget, Paperwork Reduction Project (0704-0188) Washington DC 20503.			
1. AGENCY USE ONLY *(Leave blank)*	**2. REPORT DATE** December 2001	**3. REPORT TYPE AND DATES COVERED** Master's Thesis	
4. TITLE AND SUBTITLE: Simulations of the Proposed TJNAF 100KW Free Electron Laser-Comparison With Experimental Results			**5. FUNDING NUMBERS**
6. AUTHOR Polykandriotis, Konstantinos			
7. PERFORMING ORGANIZATION NAME(S) AND ADDRESS(ES) Naval Postgraduate School Monterey, CA 93943-5000			**8. PERFORMING ORGANIZATION REPORT NUMBER**
9. SPONSORING / MONITORING AGENCY NAME(S) AND ADDRESS(ES) N/A			**10. SPONSORING / MONITORING AGENCY REPORT NUMBER**
11. SUPPLEMENTARY NOTES The views expressed in this thesis are those of the author and do not reflect the official policy or position of the Department of Defense or the U.S. Government.			
12a. DISTRIBUTION / AVAILABILITY STATEMENT Approved for public release; distribution is unlimited			**12b. DISTRIBUTION CODE**

13. ABSTRACT ***(maximum 200 words)***

One transitional step for the development of a 1 MW power directed energy weapon is the proposed l00 kW upgrade of the Thomas Jefferson National Accelerator Facility's Free Electron Laser (FEL). To improve the performance of the FEL, the use of the step-taper undulator is explored. Steady-state gain, final steady-state power, and the induced electron spread as a function of desynchronism and taper rates are determined. Comparisons are made to the conventional periodic and linearly tapered undulators. The multimode simulations used showed that the TJNAF 100kW FEL is feasible. Simulations results with Q =10 show that the inverse step-taper undulator $D = -p$ achieved the highest final power of 190 kW at a desynchronism value of d = 0.01, while maintaining the induced energy spread well below the engineering limit. The validity of our results is verified against experiments conducted in the TJNAF FEL facility. The simulations and the experimental data are in good agreement and consistent with analytic theory.

.

14. SUBJECT TERMS Free Electron Laser, desynchronism, step-taper undulator			**15. NUMBER OF PAGES** 101
			16. PRICE CODE
17. SECURITY CLASSIFICATION OF REPORT Unclassified	**18. SECURITY CLASSIFICATION OF THIS PAGE** Unclassified	**19. SECURITY CLASSIFICATION OF ABSTRACT** Unclassified	**20. LIMITATION OF ABSTRACT** UL

NSN 7540-01-280-5500 Standard Form 298 (Rev. 2-89)
Prescribed by ANSI Std. 239-18

THIS PAGE INTENTIONALLY LEFT BLANK

Approved for public release; distribution unlimited

SIMULATIONS OF THE PROPOSED TJNAF 100 KW FREE ELECTRON LASER AND COMPARISON WITH TJNAF LOW POWER EXPERIMENTS

Konstantinos Polykandriotis
Major, Hellenic Air Force
B.S., Hellenic Air Force Academy, 1988

Submitted in partial fulfillment of the
requirements for the degree of

MASTER OF SCIENCE IN APPLIED PHYSICS

from the

NAVAL POSTGRADUATE SCHOOL
December 2001

Author: Konstantinos Polykandriotis
Konstantinos Polykandriotis

Approved by: W. B. Colson
William B. Colson, Thesis Advisor

Robert L. Armstead
Robert L. Armstead, Co-Advisor

William B. Maier II
William B. Maier II, Chairman
Department of Physics

THIS PAGE INTENTIONALLY LEFT BLANK

ABSTRACT

One transitional step for the development of a 1 MW power directed energy weapon is the proposed l00 kW upgrade of the Thomas Jefferson National Accelerator Facility's Free Electron Laser (FEL). To improve the performance of the FEL, the use of the step-taper undulator is explored. Steady-state gain, final steady-state power, and the induced electron spread as a function of desynchronism and taper rates are determined. Comparisons are made to the conventional periodic and linearly tapered undulators. The multimode simulations used showed that the TJNAF 100kW FEL is feasible. Simulations results with Q =10 show that the inverse step-taper undulator $D = -p$ achieved the highest final power of 190 kW at a desynchronism value of d = 0.01, while maintaining the induced energy spread well below the engineering limit. The validity of our results is verified against experiments conducted in the TJNAF FEL facility. The simulations and the experimental data are in good agreement and consistent with analytic theory.

THIS PAGE INTENTIONALLY LEFT BLANK

TABLE OF CONTENTS

LIST OF FIGURES

LIST OF TABLES

THIS PAGE INTENTIONALLY LEFT BLANK

LIST OF SYMBOLS

A	Area
a	Dimensionless optical field
a_0	Initial dimensionless optical field
a	Absorption coefficient
B	Undula tor Magnetic Field
$\vec{b}$	Dimensionless electron velocity
$\vec{b}_\perp$	Dimensionless electron velocity in the transverse direction
c	Speed of light
γ	Lorentz factor
D	Width of the spot at target
d	Desynchronism
δ	Linear taper rate
Δ	Step taper rate
Δd	Desynchronism range
Δγ/γ	Energy spread
E_s	Electric optical field
E_e	Energy of the electron beam
e	Electron charge
f	Frequency
Φ_0	Initial flux
Φ_F	Final flux
F	Filling factor
ϕ	Optical phase
G	Gain
g	Undulator gap
$\Im$	Intensity
$\hat{I}$	Peak current
$\bar{I}$	Average current
j	Dimensionless current
K	Undulator parameter
K_e	Kinetic energy of the electron beam
k	Optical wave number
k_0	Undulator wave number
L	Undulator length
ℓ_e	Electron pulse length
λ	Optical wavelength
λ_0	Undulator wavelength
m_e	Electron mass

N	Number of undulator phase periods
$N\lambda$	Slippage distance
n	Number of electron passes through the undulator
η	Extraction efficiency
P	Power
P_e	Electron beam power
Q	Resonator quality factor
q	Charge
R	Distance
r_b	Electron beam radius
ρ	Electron beam density
S	Resonator length
Σ	Aperture area
σ_G	Electron phase velocity spread
σ_Z	Normalized electron pulse length
τ	Dimensionless time
V	Volume
ν	Electron phase velocity
ν_0	Electron initial phase velocity
u	Scalar function
w_0	Optical mode waist
θ	Angle
$z(\tau)$	Electron position
z_0	Rayleigh length
ζ	Electron phase
Ψ	Optical field parameter
Ω	Pulse repetition rate
ω	Radian frequency

ACKNOWLEDGMENTS

There are many people to whom I owe a special word of thanks for their help with this thesis. I would in particular like to thank distinguished Professor William B. Colson for his guidance and support during this research. It was a unique experience to work with an advisor who is internationally respected for his work in the field.

Helpful comments and several useful suggestions were also made by Professor Robert L. Armstead, for which I am grateful. A special debt is owed to Mr. Joe Blau. His assistance was more than necessary for the completion of this work. I also want to thank Professor Peter Crooker of the Hawaiian University for his helpful suggestions.

Finally, I thank my wife Katerina because without her patience, encouragement and support this thesis would not have been possible.

THIS PAGE INTENTIONALLY LEFT BLANK

EXECUTIVE SUMMARY

The Free Electron Laser (FEL) weapon is excellent for providing state-of-the-art air defense. It is also effective, if need be, in offensive operations. It is possible for this weapon system to achieve a soft kill whenever needed by adjusting lethality. When combined with its accuracy makes it a valuable tool in operations where the requirement is not to only win, but also to avoid casualties.

One transitional step toward the l MW output power required for a laser weapon is the proposed l00 kW upgrade of the Thomas Jefferson National Accelerator Facility's FEL. At present, the TJNAF FEL is the most powerful FEL in the world and operates at more than 2 kW average power.

Our multimode simulations showed that this development is feasible, and for the current TJNAF 100kW FEL parameters with $Q = 4.2$, the inversely tapered undulator $\Delta = -p$ achieved the highest final power at a desynchronism of $d = 0.04$. The output power produced was $P \sim 120$ kW, which is above the 100kW objective. The small values of the induced electron energy spread (~3.5%) made it possible to explore a design with lower 10% losses of ($Q = 10$) in an optical cavity. The higher Q factor was chosen to increase the efficiency of the system, while maintaining the induced energy spread well below the 15% engineering upper limit. Simulations results with $Q = 10$ design indicate that the inverse step-taper undulator $\Delta = -p$ achieved the highest final power $P = 190$ kW at a desynchronism of $d = 0.01$. The inverse linear taper $d = -2p$ achieved the highest final power $P = 200$ kW at a desynchronism of $d = 0.01$. For all the aforementioned cases the steady-state gain, the final steady-state power, and the induced electron spread as a function of desynchronism and taper rates were determined.

The validity of our results was verified against experiments conducted in the TJNAF FEL facility at lower power. FEL operation as a function of various taper rates and desynchronism values was studied. The purpose of the simulations was to compare experimental observations with theoretical analysis, and, by using a wider range of

parameters than allowed in the experiment, to extract more physical meaning from the results.

The simulations and the experimental data agreed well and for the most part were consistent with analytic theory. This theory indicates that as the taper increases, the desynchronism width decreases. The experiment shows this trend, but not as clearly as the simulation data. Only one point shows a significant deviation between the simulation and experiment. This has resulted in more examination of the experimental data, revealing that the conditions changed during the measurement of the point in question.

The maximum gain with no tapering, $d = 0,$ occurred, as would be expected. As the taper rate d increases or decreases, the gain decreases from 160% to about 40% symmetrically around $d = 0.$ At positive or negative taper rates near $d = \pm 8p$, the gain plateaus observed decreased much more slowly with an increasing taper rate. As the taper rate increases in magnitude from $|d| = 8p$ out to $|d| = 24p$, the gain decreases from about 40% down to about 10%. The gain plateau at large values of taper begins at a value of taper d that causes the gain spectrum to change shape so that there are two peaks with nearly the same peak gain. As the taper is increased and the peak available gain decreases, the gain spectrum acquires multiple peaks with comparable gain. As the primary gain peak decreases, other surrounding gain peaks increase in comparison. This can also occur in the untapered case, but results in a smaller gain peak. As the peak available gain increases, or decreases, at any value of tapering, the desynchronism curve width Δd increases or decreases correspondingly. With more gain available there are more values of desynchronism that are above the threshold which makes the desynchronism curve wider.

I. INTRODUCTION

Directed energy weapons (DEW) is not a new initiative that "just appeared." It is the consequence of changes in political philosophy and technology. The emergence of more and more power sources of microwave energy is clearly a key factor in their applicability. Furthermore, many of these sources are available at reasonable cost and satisfactory sizes.

DEWs have been on the on the U.S. military's "love to have" list for several decades. Within the United States, all three services have been actively developing laser technology. One of the most impressive land-based Tactical High-Energy Lasers (THEL) is the "Nautilus". It is a joint U.S. Army and Israeli project, which uses a Mid-Infra-Red Advanced Chemical Laser (MIRACL). At present, it is being tested at White Sands Missile Range in New Mexico and has been successfully tested against the supersonic BM-21 122mm artillery rocket. The Nautilus program is still being tested and reached a milestone when, in June 2000, a test firing resulted in the destruction of a Katyusha type missile in flight [Ref. 1].

The U.S. Air Force, as well as the U.S. Army, in conjunction with the Air Borne Laser (ABL) program, adapted the chemical-oxygen-iodine laser (COIL) to a flyable model against missiles. This project, which was on schedule and within budget, is now transitioning from the early concept design to operational use.

The U.S. Navy is also interested, and on the 24th of April 2001 the Commander in Chief of the U.S. Atlantic Fleet sent the following letter to the Chief of Naval Operations:

> …and has proven that Speed of Light weapons can be very effective against these small high speed threats. Such a laser weapon would offer our Naval forces an extremely versatile weapon to counter numerous soft and hard targets. A High Energy Laser weapon can be designed to deliver energy that can track, warn, damage, mission kill, and if need be, destroy a threat. I believe it is exactly this type of weapon system that our forces need in the littoral environment where, even though the threat may not always be as sophisticated as a highly maneuverable cruise missile, intentions are often more difficult to discern and timelines are extremely short ……

A Free Electron Laser (FEL) as a weapon is an excellent approach to fulfilling present and future requirements. It could provide state-of-the-art air defense not only to ships but also to sensitive areas such as Naval and Air Force Bases. It is capable of achieving a high-probability hard kill against all cruise missiles. It increases the engagement range and minimizes engagement time and thus reduces the threat of simultaneously arriving cruise missiles. Reliability is almost l00%. Since only light and vacuum are involved in the weapon system, minimal maintenance is required. Its infinite magazine, its instantaneous reaction at the speed of light time and the rapid re-engagement point offer many advantages over gun and missile-based close-in weapons.

It is also possible for this weapon system to achieve a soft kill whenever needed by adjusting the lethality. The latter, combined with its pinpoint accuracy, makes it a valuable tool in operations where the requirement is not to only win, but also to avoid casualties [Ref. 2]. This fact is present in all peacekeeping operations, as it was in Kosovo and now in Afghanistan. This philosophy has been another push toward the deployment of DEWs and FELs.

Presently, FEL research is widespread and advancing on many fronts. The impetus comes from some unique advantages the device offers over other types of lasers. [Ref. 3]:

- "Potential for producing very high power by extending technology developed for existing electron accelerators. The evolution of power densities in magnetrons, klystrons and gyrotrons have reached their limits while the limit for FELs have not yet been reached as Figure 1 indicates. There the product of the average power and the square of the radiation frequency, as a figure of merit, is shown. These available microwave powers were unthinkable just a few years ago.
- Prospects for wall-plug efficiency more than 10 percent or more at high powers.
- Potential for tunable operation from the millimeter-wave region to the extreme-ultraviolet or soft x-ray region, although no single device would operate over such a broad range. (The broad tuning range comes from the fact that the electrons are not bound when they emit light; it would be achieved by varying the electron energy and the spacing and strength of the magnetic field)"

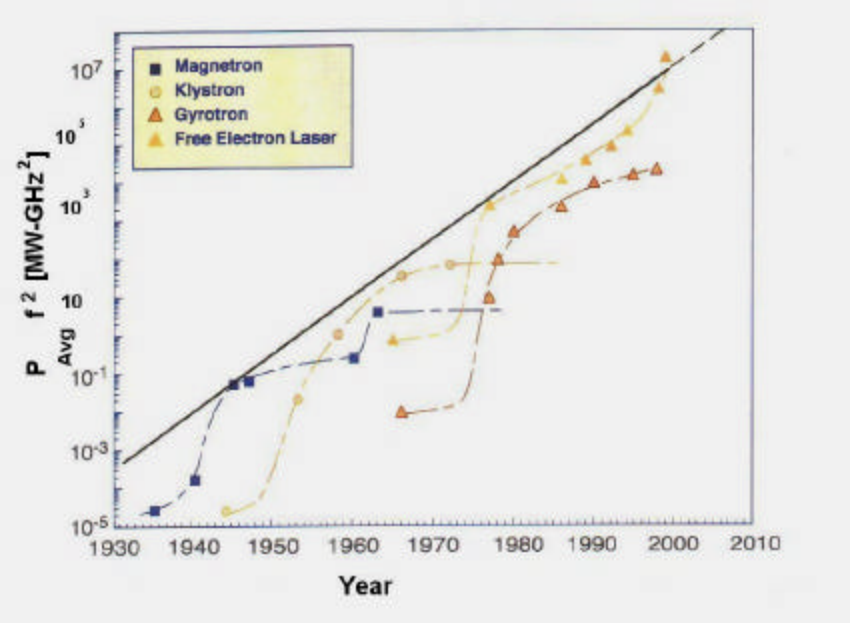

Figure 1. Progress in the Development of a Variety of Vacuum Electronic Sources of Coherent Radiation as Measured by the Evolution of the Product of the Average Power and the Square of the Frequency. "From [Ref. 4]."

Chapter II of this thesis describes the FEL weapon concept and the improvements gained in the field. Present limitations mentioned at the Workshop 2001 in Virginia, USA, compare the FEL with other weapons (HEL and conventional) and address its benefits.

Chapter III gives an overview of the theoretical background and discusses the physics behind the FEL.

Chapter IV describes the results of simulations for the proposed l00 kW upgrade to the TJNAF FEL. This upgrade is a transitional step for the l MW output power. This work was originally presented at the 23rd International FEL Conference in Darmstadt, Germany and has been accepted for publication in Nuclear Instruments and Methods in Physics Research.

Chapter V presents the analysis of simulation results based on experiments conducted at TJNAF. Simulations and experimental results are compared to analytical theory.

THIS PAGE INTENTIONALLY LEFT BLANK

II. FEL

The FEL is a device which extracts light energy from a beam of relativistic electrons passing through a spatially periodic magnetic field. John Madey first introduced the concept in 1970 [Ref. 5]. It is unlike other lasers, such as solid-state, semiconductors and liquid lasers, because it relies on light emitted by electrons that are not bound to atoms.

An FEL consists of an electron beam source, a periodic transverse magnetic field (an "undulator" or "wiggler" magnet), and an optical resonator as shown in Figure 2.

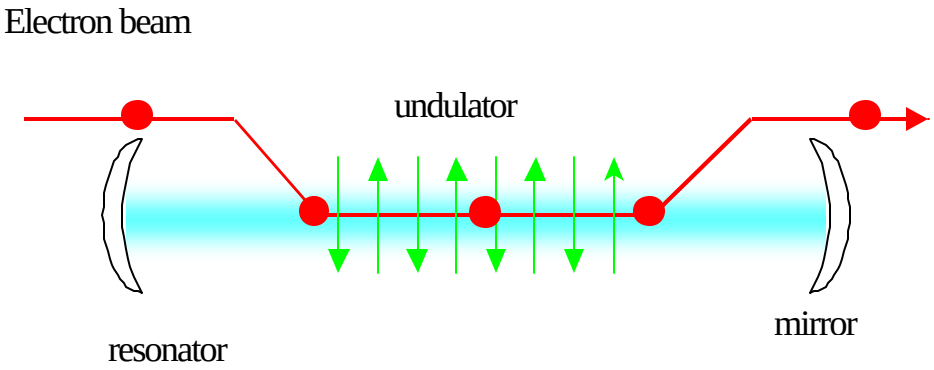

Figure 2. The FEL Schematic.

The undulator magnet in an FEL imposes a transverse acceleration on the electrons, resulting in the generation and amplification of light, which co-propagates with the electron beam through the magnet. As in a conventional laser, the resonator mirrors provide feedback around the amplifying medium, permitting the stored radiation to build up to saturation and produce a very powerful, coherent laser beam.

A. WEAPON CONCEPT-PRINCIPLES INVOLVED

1. The Way the Target is Destroyed

A laser beam in the basic fundamental mode closely approximates a Gaussian. The intensity drops off from a maximum and has no side lobes. The typical laser beam is quite narrow at no more than a few millimeters in diameter. Furthermore, when operating at that mode, the minimum waist of the optical beam is where the highest energy density occurs.

Since the beam resembles a truncated plane wave, it is, of course, highly spatially coherent. Its directionality may be thought of as a manifestation of that coherence. Laser light is quasimonochromatic, and generally has an exceedingly narrow frequency bandwidth indicating that it is highly temporally coherent. Another attribute is the amount of radiant power that can be delivered in that narrow frequency band. The laser is distinctive in that it emits all its energy in the form of a narrow beam. In contrast, a 100W incandescent light bulb may give out considerably more radiant energy than a lower-power cw laser, but the emission is incoherent, spread over a large solid angle with a broad bandwidth.

A good lens can totally intercept a laser beam and focus all of its energy into a minute spot whose diameter varies directly with wavelength l . Spot diameters of just a few thousandths of an inch can readily be attained with lenses that have a conveniently short focal length. The laser intensity that can readily be generated in a focused beam is over 10^{17} W/cm^2, in contrast to an oxyacetylene flame having an intensity of roughly 10^3 W/cm^2. A focused laser beam of a few kilowatts can burn a hole through a quarter-inch stainless steel plate in about 10 seconds. [Ref. 6]

Studies and scaling experiments have shown that a liter of a missile's material can be destroyed in a few seconds with 1 MW of laser power [Ref. 7]. One liter corresponds to a hole with the dimension 10cm x 10cm x 10cm which is generally enough to structurally disable the missile. Missile destruction can be achieved in different by an explosion of the missile warhead, or an aerodynamic instability causing the missile to breakup.

A targeting system on a launching platform will control the beam directed to the missile and burn a hole in it. Unlike conventional bullets or missiles, light instantly travels to the target and does not suffer from gravitational effects. The Acquisition Tracking and Pointing (ATP) system is in use and has been successfully tested in the MIRACL project many years ago [Ref. 1]. Acquisition includes the detection of the target in the tracking system using infrared radiation. Tracking begins when a series of consecutive observed positions collected to allow for the filing of the azimuth, elevation and time. Connecting these points permits the construction of nominal track data that

point the telescope in order to keep the image of the target centered in the tracking focal plane. The system temporal response, which includes a camera processor and motors, must be fast enough so that the target does not disappear from the camera field of view. The pointer/tracker will be stabilized against unintended motion by using a high speed gyroscope and inertial measurement system. ATP could cost $6 million, including the multiple target acquisition sensor and stabilization system [Ref. 8].

2. The Threat - Requirements from a Weapon

Targets are evaluated with respect to their maneuverability, size, and vulnerability to attack. Target maneuverability imposes a requirement that the missile must be capable of terminal maneuverability to effect lethality.

The airborne-target spectrum is quite varied and consists of low altitude, slow-moving targets in ground clutter, high-altitude fast-moving targets, head-on targets with tremendous closing speeds and side-encounter targets with high-g turning requirements. If the threat is other than airborne-targets, no known limitations are implied. In contrast, the surgical accuracy of the system, the absence of fragments and the instant battle assessment make the system operable for many targets and environments. Range and time-to-range is a factor that does not greatly affect the FEL weapon design. The engineer need not consider design features affecting range and time-to-range such as drag, wings, controls, lifting surfaces, and other parasitic losses. The incredibly small time of flight of 33 μsec, or the time it takes the beam to reach the missile at 10 km, is the key issue. However, environmental constraints and atmospheric transmittance have to be taken into account.

Cost per shot must be much less than cost of threat target, with high lethality per shot. For example, an Unmanned Aerial Vehicle (UAV), which is used for reconnaissance, may be worth less than an expensive sea-sparrow missile. The motivation for cheap, effective defense does not imply that we are not going to use all the means of defense, whenever human lives are placed in danger. Additionally, the individual engagement time must be short in order to engage a large number of targets. A dwell time of 3 seconds makes it possible to handle several incoming supersonic targets simultaneously.

3. FEL Comparison with Existing Weapons

Present systems detection is limited to the horizon for low level flying threats. Unlike the antiballistic-missile kinetic kill systems designed for missile-terminal phase-defense, the FEL mode of attack offers several key advantages. First, the target is much slower moving and there is less urgency for targeteers to worry about distinguishing decoys. Additionally, a significant advantage of the FEL is that it is environmentally friendly as it does not generate the toxic effluents common to other types of weapons. This issue of "the exhaust gas contaminants" is serious since the crew could be harmed, and equipment damaged. Furthermore, another disadvantage is the need for a logistics supply of hazardous and toxic chemicals. The latter probably is the strongest disadvantage since no one today wants to handle such materials.

With pinpoint accuracy, FELs can destroy precise targets in rapid order, while not harming non-military facilities and people. This is a benefit when compared with other weapons, which often destroy more than the intended target. Thus, the damage to surrounding populations and facilities is minimized.

With an almost zero reaction time, FELs enhance the survivability of the user, especially in cases when the threat is unexpected. This reaction time at long range disables the enemy threat before getting near. Current close-in weapons, such as the Phalanx gun, suffer from dispersion as a result of vibrations. Moreover, simulations and demonstrations have shown that the probability of hitting the missile reduces as range increases. The Phalanx does not destroy the missile at a distance sufficiently far enough away to protect the ship and the crew from serious damage [Ref. 9].

The Rapier, used in the 1982 Falklands campaign, the Hawk, and the Arrow systems are deployed worldwide. They can provide short-range air defense of airfields and smaller troop concentrations. These systems are more than 20 years old, and even the famous Patriot air defense system is not as good as thought to be. "Patriot wasn't what I would call highly effective. We lost some lives to ballistic missiles during Desert Storm. Twenty-six Army soldiers were killed in the barracks in Dhahran as a result as an attack from a Scud missile" as stated by Lt. Gen. Lester L. Lyles [Ref. 10].

FEL is designed in such a way that maintenance is minimal. It can be fired instantly and no other maintenance is needed. Furthermore, it could play a role as a "weapon of choice" in today's U.S. military because it has the ability to set power levels on a graduate scale and provide the user with choices unavailable in kinetic energy weapons as well the ability to minimize casualties by permitting a selection of non-lethal options. It has speed-of-light engagement with a variety of targets and has the potential to produce a range of precisely controlled effects, as well as the potential for deep magazines and low cost per shot. The absence of costly rounds or defensive intercept missiles causes the cost per shot to drop to ~ $2/missile (using 1gal of fuel), while the RAM is ~$0.7 millions/missile and the PHALANX is ~$3k/missile.

B. FEL DESIGN

1. Application

The application requires high power in a small footprint. The proposed FEL consists of six basic components: the electron injector, the linear accelerator, the undulator, the resonator, the refrigerator and the electron beam dump. All these components can be packaged into a box with dimensions of 12m x 4m x 4m as shown in Figure 3.

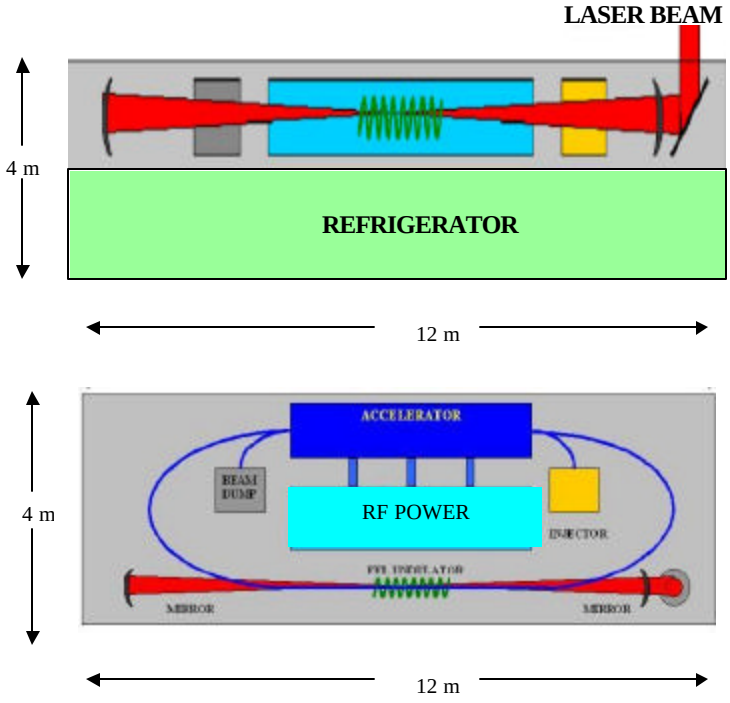

Figure 3. FEL MW Design. (After [Ref. 11]).

The configuration and operational parameters are provided in Table 1.

Electron beam energy	E_e =140 MeV
Relativistic Lorentz factor	g = 275
Average current	$\overline{I}$ = 0.6 Amp
Accelerator RF frequency	W =750 MHz
Accelerator gradient	17 MeV/m
Peak current	$\hat{I} = 800$ Amp
Charge	q = 0.8 nC
Electron beam radius	r_e = 0.08 mm
Electron beam density/pulse	r = 8×10^{14} /cm^3
Optical mode waist radius	w_o = 0.08 mm
Number of undulator periods	N = 20
Undulator period	l_o = 3 cm
Undulator length	L = 60 cm
Undulator gap	g = 1 cm
Undulator parameter	K = 2
Resonator length	S =12 m
Optical wavelength	l =1 μm
Quality factor	Q = 4
Extraction efficiency	$h \approx 1/4N = 1.25\%$
Energy spread	$\Delta g / g \approx 2/N = 0.1\%$
Rayleigh length	z_o = 1.8cm
Intensity on mirrors	210 kW/cm^2
System dimensions	12mx4mx4m
Weight	60 Tons
Cost	$60 million

Table 1. MW FEL Parameters. (From [Ref. 11])

Some of the challenging issues are intensity in the mirrors, effective recirculation of the 84 MW electron beam and beam transportation. A deployable MW-class FEL will need a sophisticated feedback, control and diagnostic system. Due to the short turn-on time and limited mission duration, the system must be self-diagnosing, and self-correcting for shock and vibrationally induced misalignments. [Ref. 12]

2. Atmospheric Propagation

Although powerful at the point of origin and delivered at more than 186,000 miles per second, a laser's energy can be absorbed and diffused even in a relatively short passage through the atmosphere. There are propagation issues that need to be considered:

- Thermal blooming,
- Absorption,
- Diffraction,
- Scattering.

It is possible to overcome these difficulties by the use of scaling laws and various simulations to predict what will happen in the MW class. These tools have limited applications as scaling and simulations do not always provide reliable results. The use of adaptive optics is another issue which may be consider in our case.

a. Thermal Blooming

Random temperature variations caused by turbulence take place when a high power optical beam travels through the atmosphere. As a result, the refractive index changes randomly and forms random lens along the beam path. This causes the optical beam to spread as it goes through the turbulent atmosphere. Thermo blooming is the laser-induced absorption-driven heating which spreads the beam core. Blooming is nonlinear and depends not only on medium composition and density but also on beam properties as well such as wavelength, pulse length and intensity. Adverse weather conditions, humidity, absence of cross winds and the smoke from combat environments can also degrade the beam quality.

b. Absorption

One of the major limitations of the transfer of laser energy from the source to the target is the absorption of the laser's energy by the earth's atmosphere. Light passing through an optical system can be attenuated by absorption as shown in Figure 4.

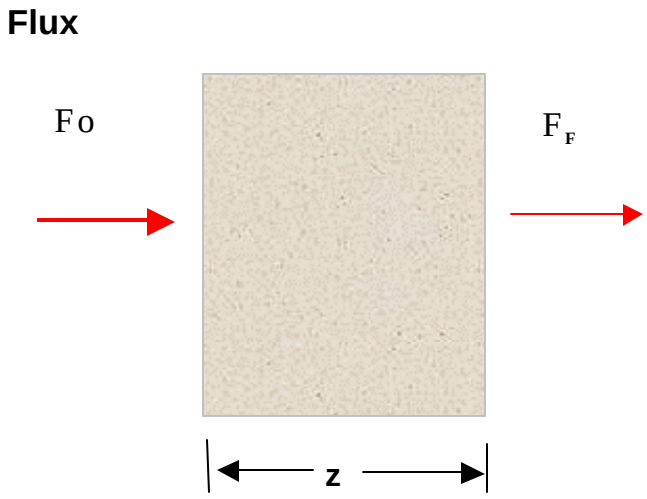

Figure 4. Light Absorption.

The exponential law of absorption is the basic working relationship, but specific terms such as absorbance and transmittance are widely used as well. The differential absorption can be expressed as

$$d\Phi = -a\Phi dz \tag{2.1}$$

where a is the absorption coefficient and which upon integration from 0 to z gives the exponential law of absorption:

$$\frac{\Phi_F}{\Phi_0} = e^{-a z} \tag{2.2}$$

c. Diffraction

Diffraction limits affects propagation over a large distance and therefore has to be taken into account. For distances larger than the Rayleigh length, $z > p w^2 / l$, where w is the radius of the source aperture, we are able to use the Fraunhofer approximation. At a wavelength of 1.0 μm and an aperture width of 2.5 cm (1 inch), this distance is $z > 1250$ meters. If we deal with a circular aperture, the intensity distribution can be written as [Ref. 13]

$$\Im(r) = \left(\frac{A}{l z} \right)^2 \left[2 \frac{J_1(kwr / z)}{kwr / z} \right]^2 . \qquad (2.3)$$

where $A = p w^2$, w is the radius of the source aperture, J_1 is the Bessel function of order 1, and r the radius coordinate in the observation plane. The intensity distribution in Equation (2.3) is referred to as the Airy pattern after G. B. Airy who first derived it. Since $\sin q = r / z$, the irradiance can be written as a function of q, and Equation (2.3) gives the intensity $\Im$ at distance z equal to

$$\Im = 4\Im(0) \frac{J_1^2 (kw \sin q)}{(kw \sin q)^2}. \qquad (2.4)$$

The fundamental mode (TEM_{00}), from a circular aperture, is shown in Figure 5.

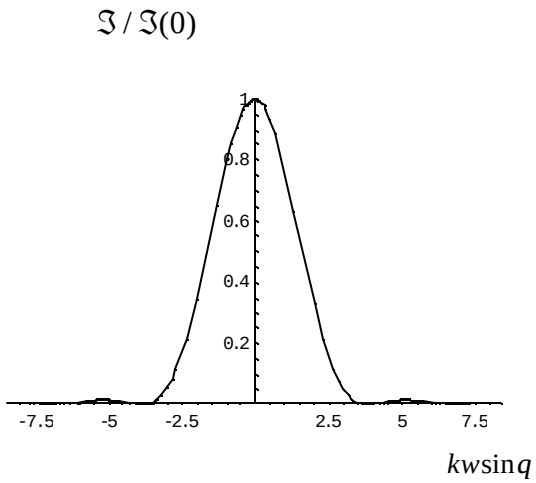

Figure 5. Intensity Pattern for Circular Aperture.

To find the width of the central lobe, measured along the horizontal axis, the numerator of Equation (2.4) where it is zero (1st of minima) must be found. From tables, it can be seen that $J_1(u) = 0$ when $u = 3.83$ so that the width of the central lobe at distance z is

$$D = 1.22 \frac{l z}{w}. \qquad (2.5)$$

Equations (2.3) and (2.5) strongly suggest short wavelength for a directed energy weapon as the intensity at the target is inverse proportionally of the square of the wavelength, while the width where the beam is focused is proportionally to the wavelength. Furthermore, circular apertures are preferable as 84% of light arrives within the central lobe (Airy disk), and 91% within the bounds of the second dark ring [Ref. 6]. For the FEL weapon with $l = 1$ μm wavelengths laser light from a $w = 0.2$ m aperture on the ship, the spot size at range $z = 5$ km could be as small as $w_T =$ cm. To avoid thermal blooming, to damage a larger target area, the beam only will be focused to a 10 cm spot. Diffraction at $l = 1$ μm is not a problem.

d. Scattering

Rayleigh scattering refers to the scattering of light off molecules in the air, and from particles up to about a tenth of the wavelength of light. The strong wavelength dependence of Rayleigh scattering favors the short wavelength l since the scattered intensity I is proportional to l^{-4} [Ref. 14]. For example the Rayleigh scattering at 400 nm is 40 times greater than at 1μm for equal incident intensity.

For particles sizes larger than a wavelength, Mie scattering predominates. This scattering produces a pattern like an antenna lobe, with a sharper, more intense forward lobe for larger particles. Mie scattering is not strongly wavelength dependent. Both scattering types are presented schematically in Figure 6.

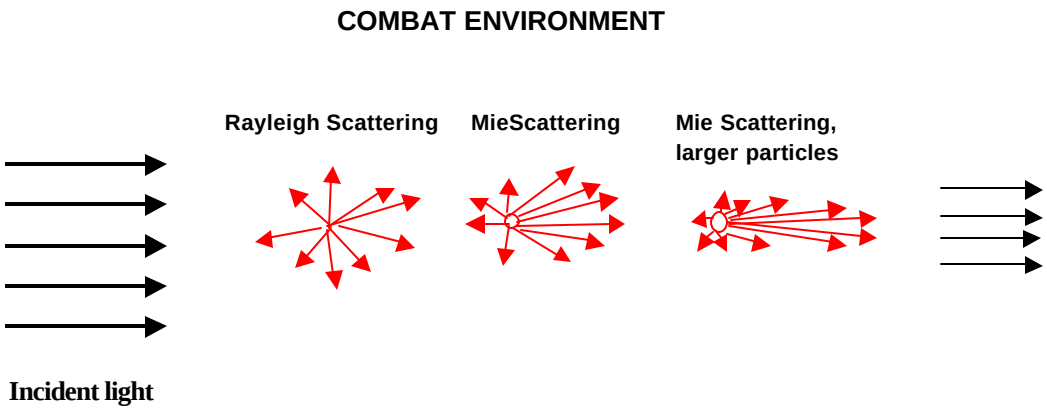

Figure 6. Scattering from Air Molecules.

The atmospheric transmittance over a wavelength range is a complex problem and extremely crucial to directed energy because it determines the choice of a suitable wavelength. Absorption-driven thermal blooming, scattering and turbulence can be major limitations to performance and can lead to the dispersion of the beam power.

The atmospheric transmittance problem has been described by computer modeling codes such as FASCODE, LOWTRAN, MODRAN and MOLLY. All the above codes allow the user to insert weather conditions and to select from several different environments. MOLLY is a time-dependent computer simulation of adaptively compensated laser propagation through turbulence and thermal blooming. A graph of typical atmospheric transmittance versus wavelength using this simulation is shown in Figure 7. Notice there are specific windows where the attenuation is much less, and therefore it is preferable to operate the laser in those regions.

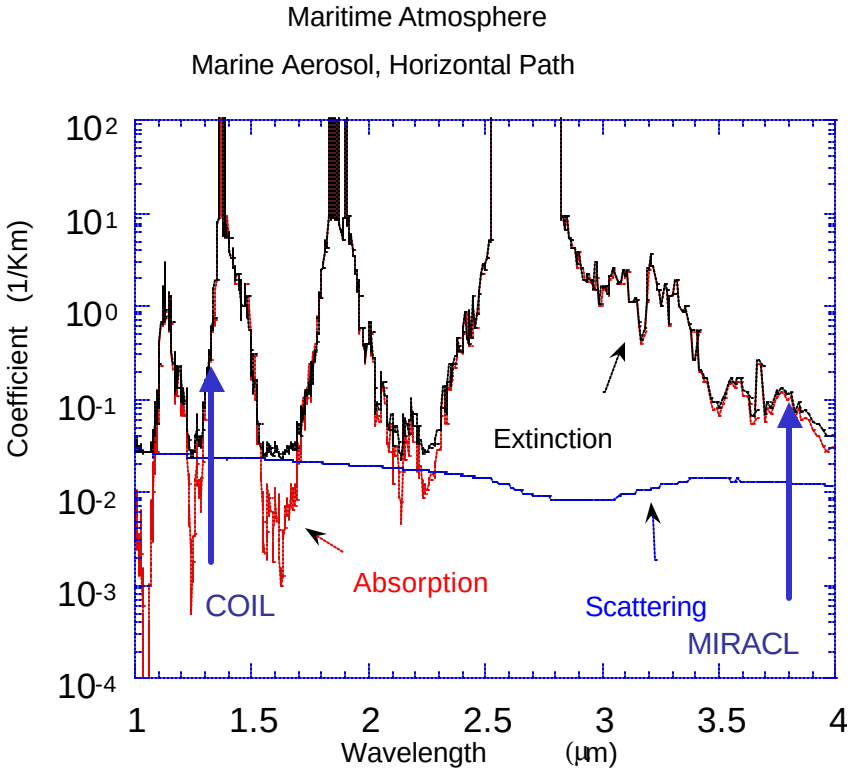

Figure 7. Atmospheric Transmittance (From [Ref. 15]).

As can be seen from the above figure, both COIL and MIRACL lasers perform poorly in a maritime environment and suffer from absorption. Wavelengths

$l = 1.06\,\mu m$, $l = 1.25\,\mu m$, $l = 1.62\,\mu m$ are attractive for the MW-class because as the absorption coefficient is small, $a \le 0.001 km^{-1}$. For the value of $a = 0.001 km^{-1}$ we have almost no reduction of the initial power, see Equation (2.2), and $\Phi_0 \approx \Phi_F$. Note that the width of each window is relatively small (~0.2μm), and a small deviation causes excessive dissipation and spreading due to atmospheric conditions, which results in degraded range and beam quality.

3. Adaptive Optics

Current acquisition and pointing systems are capable of tracking maneuverable supersonic targets and holding the optical beam to a small area of~100cm^2. Adaptive optics can be used to transfer the lethal beam and focus it in. In addition, adaptive optics are used to overcome propagation affected by turbulence.. The advantage of using adaptive optics is shown in the simulations results in Figure 8.

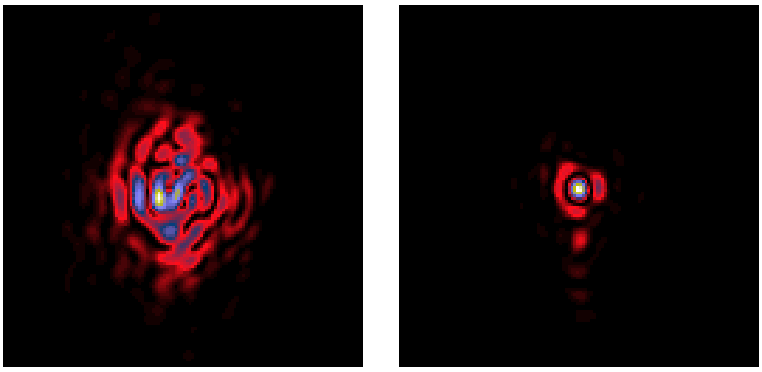

no adaptive optics adaptive optics

Figure 8. Function of Adaptive Optics (from [Ref. 15]).

On the left hand side, no adaptive optics are used and thermal distortions in the atmosphere spread the laser beam. On the right hand side the improvement is obvious after the application of adaptive optic mirror at source. Thermal distortions and moderate thermo blooming are largely corrected and allow the delivery of the lethal beam to the target. The system performance is degraded if the thermal distortions and the thermo blooming effect are more than moderate. In the FEL application discussed here, turbulence is much less than shown in Figure 7 so that adaptive optics may not be

required. If it is required the adaptive optics adds a cost of $3M to the entire FEL system [Ref. 8].

C. FEL SAFETY

1. Radiation Concerns

Radiation shielding is required for the electron beam dump. The FEL with the energy recovery system allows the electron beam to reenter the RF cavities 180 degrees out of phase with the accelerating fields. This energy is recovered as RF power and used to accelerate subsequent electron pulses to repeat the cycle. The residual energy after deceleration is about 7 MeV [Ref. 16] and is below the threshold of generating neutron radiation when it is dissipated in the beam dump. Only beryllium (Be) and Osmium (Os) have a neutron production threshold below 7 MeV and therefore, as long as beryllium and osmium are excluded from beam dump structural materials, neutron generation is not an issue [Ref. 17]. Without the production of neutrons, much less shielding is required. Other human safety issues include the need for eye protection when personnel may be topside or have visual access to the topside scattering off the sea surface during an engagement. In such cases, safety goggles may be required [Ref. 18].

2. Helium Concerns

The cryogenic systems require the use of liquid helium. Helium is non-flammable, non-corrosive, non-toxic and not listed as a marine pollutant by Department of Transportation (DOT). When the FEL is running properly, the helium is in a closed loop refrigerator and totally contained. Thus, there are no safety concerns. However, because the helium is cryogenic, a vacuum is used to insulate the piping and storage containers (dewars). If a major vacuum leak should occur, the helium boils off quite rapidly leading to safety concerns:

- It can over pressure the storage tank or piping since helium expands 750 times when going from a room temperature liquid to a gas. If a suitable way is not provided for the gas to escape, the vessel could explode.
- If the expanding gas should come into contact with someone, cryo-burns can occur because it is very cold when first released.
- If the helium goes into a confined space, it can displace the oxygen and lead to suffocation of personnel in those compartments. If air with less than 12% oxygen is breathed, unconsciousness can occur in 9 seconds with brain damage occurring in 5 minutes. If the level drops to 8%, death is imminent in minutes.

The precautions are:

- Provide burst disks on the system connected to a vent so the helium can safely escape.
- In the case of an expanding plume, do not stick a body part into it. Protective clothing is required.
- Provide a means for the helium to escape if it wants to rise. If there is a pipe in the ceiling, it will escape up the pipe and disperse. To prevent leakage into other compartments have a ledge at the top of the door below the ceiling level to prevent the flow. Also, oxygen monitors on the ceiling to send out an alarm if oxygen levels drop below 18% are required.

The total volume of liquid helium in the linear accelerator will be less than 5000 liters, making approximately 5 megaliters of gas available which could easily fill a room with 155m^3 volume. Nevertheless, helium is much safer than liquid nitrogen. It goes to the ceiling and escapes. Nitrogen goes to the floor and cannot be seen once it warms [Ref. 19]. Helium vents would be included in the weapon design.

D. CONCLUSIONS

1. Challenges

Theoretical calculations have shown that FELs have the potential to scale to megawatts, but it is an engineering challenge to improve reliability and reduce the size and the cost of an FEL. For instance, a critical concern is improving electron-beam brightness as beam current is increased. Additionally, new functions must be introduced into FEL technology to advance the MW system. The radius of curvature of the resonators mirrors and a cooled sapphire window must be controlled to tight tolerances. Furthermore, atmospheric propagation effects, and the thresholds at which these effects are significant, must be well understood. This understanding will, to a large extent, define the required laser weapon system. Performance, downsizing and cost are also crucial considerations and are illustrated in Figure 9.

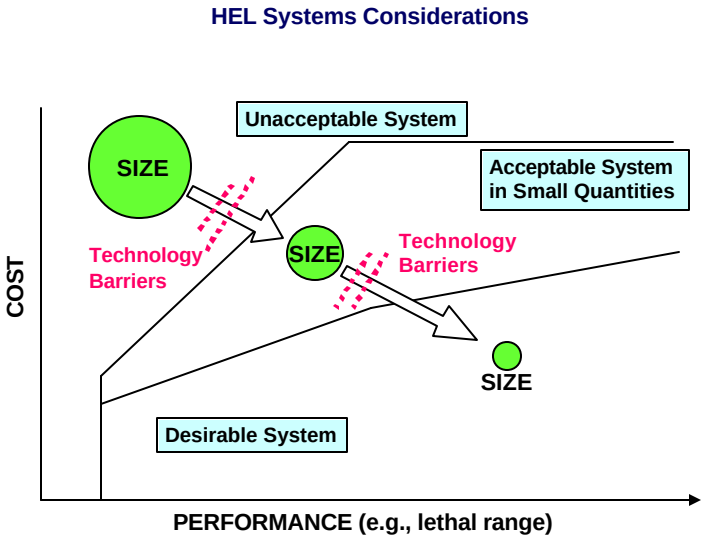

Figure 9. Acceptable System Diagram (After [Ref. 20]).

After the workshop in Virginia in June 2001, the synopsis is that a MW-class infrared free-electron laser (IRFEL) appears to be a challenging, but feasible, proposition [Ref. 21].

2. Resources Required

The DoD investment strategy is to fund those technologies that have the potential to penetrate and bypass identified technology barriers. In practice, in the face of funding pressures, inadequate funding is being provided to a wide variety of programs. These programs should be replaced with focused, sequential developments funded at the level of effort needed to create real progress. It is also believed that considerably more funding on the level of $100-150 million per year is needed [Ref. 22].

Currently, the money spent in this area in FY01 was $30 million, while the funding for the DoD high-energy laser programs was $474 million [Ref. 20]. Studies at TJNAF and simulations presented in Chapter IV have indicated that scaling the system to 100 kW of power is feasible and straightforward. Funding is already being supplied by the Office of Naval Research (ONR) and additional funding is expected from the U.S. Air Force.

THIS PAGE INTENTIONALLY LEFT BLANK

III. THE PHYSICS BEHIND FEL

A. INTRODUCTION

A free electron traveling undisturbed will not spontaneously emit energy. However, if the electron accelerates, it must absorb energy. If it decelerates, it must radiate energy. For example, if an electron increases its velocity in a particle accelerator, it does so by absorbing energy from an RF electromagnetic field supplied by the accelerator. Its kinetic energy is

$$K_e = (g - 1)m_e c^2 \tag{3.1}$$

where g is the Lorentz factor and m_e is the electron rest mass. The term $m_e c^2$ is called rest energy (0.511 MeV). The Lorentz factor g is given by

$$g = \frac{1}{\sqrt{1 - \vec{b} \cdot \vec{b}}} \tag{3.2}$$

where $\vec{b} = \vec{u} / c$ is the dimensionless electron velocity.

In an FEL, the electron trajectory is directed with bending magnets into the undulator. Along the path of the undulator, the electron starts to wiggle in the transverse direction as soon as it passes through each alternating magnetic field. During the wiggling, the electron emits radiation into a narrow cone of opening angle J [Ref. 23], where

$$J = g^{-1} \tag{3.3}$$

This type of radiation should be distinguished from *Bremsstrahlung* or broad band synchrotron radiation which usually consists of several harmonics in addition to the fundamental [Ref. 24]. This thesis deals primarily with a pulsed FEL operated as an oscillator. A radio-frequency (RF) electron-gun is used to inject electron pulses into the accelerator. The radiation is stored in a cavity and amplified over many passes. Other types of FELs either use continuous wave (CW) power or amplify the radiation in a single pass and are called amplifiers [Ref. 25]. Table 1 lists not only the different types, but also the design parameters for existing and proposed FELs [Ref. 26].

Relativistic Short Wavelength Free Electron Lasers (2000)

FELs	λ(μm)	σ_z	E(MeV)	I(A)	N	λ_0(cm)	K(rms)	Acc.,Type[Ref.]
EXISTING ======	-------	-------	-------	-------	-------	-------	-------	-------
UCSB(mm FEL)	340	25μs	6	2	42	7.1	0.7	EA,O[1]
Dartmouth(FEL)	200	CW	0.04	0.001	50	300	-	SP,O[2]
Korea(KAERI-FEL)	97-150	25ps	6.5	0.5	80	2.5	1.6	RF,O[47]
Himeji(LEENA)	65-75	10ps	5.4	10	50	1.6	0.5	RF,O[3]
UCSB(FIR FEL)	60	25μs	6	2	150	2	0.1	EA,O[1]
Osaka(ILE/ILT)	47	3ps	8	50	50	2	0.5	RF,O[4]
Osaka(ISIR)	40	30ps	17	50	32	6	1	RF,O[5]
Tokai(JAERI-FEL)	22	5ps	16.5	100	52	3.3	0.7	RF,O[6]
Bruyeres(ELSA)	20	30ps	18	100	30	3	0.8	RF,O[7]
Osaka(FELI4)	18-40	10ps	33	40	30	8	1.3-1.7	RF,O[8]
UCLA-Kurchatov	16	3ps	13.5	80	40	1.5	1	RF,A[9]
LANL(RAFEL)	15.5	15ps	17	300	200	2	0.9	RF,O[10]
Stanford(FIREFLY)	15-65	1-5ps	15-32	14	25	6	1	RF,O[11]
UCLA-Kurchatov-LANL	12	5ps	18	170	100	2	0.7	RF,A[12]
Maryland(MIRFEL)	12-21	5ps	9-14	100	73	1.4	0.2	RF,O[13]
Beijing(IHEP)	10	4ps	30	14	50	3	1	RF,O[14]
Darmstadt(IR-FEL)	6-8	2ps	25-50	2.7	80	3.2	1	RF,O[15]
BNL(HGHG)	5.3	6ps	40	120	60	3.3	1.44	RF,A[16]
Osaka(FELI1)	5.5	10ps	33.2	42	58	3.4	1	RF,O[17]
Tokyo(FEL-SUT)	5-16	2.5ps	32	0.2	40	3.2	0.7-2.5	RF,O[48]
Nieuwegein(FELIX)	4-200	1ps	50	50	38	6.5	1.8	RF,O[18]
Duke(MarkIII)	3	3ps	44	20	47	2.3	1	RF,O[19]
TJNAF(FEL)	1-6	0.4ps	48	60	41	2.7	0.9	RF,O[20]
Stanford(SCAFEL)	3-13	.5-12ps	22-45	10	72	3.1	0.8	RF,O[21]
Orsay(CLIO)	3-53	0.1-3ps	21-50	80	38	5	1.4	RF,O[22]
Vanderbilt(FELI)	2.0-9.8	0.7ps	43	50	52	2.3	1	RF,O[23]
Osaka(FELI2)	1.88	10ps	68	42	78	3.8	1	RF,O[17]
BNL(ATF)	0.5	6ps	50	100	70	0.88	0.4	RF,O[24]
Dortmund(FELICITAI)	0.47	50ps	450	90	17	25	2	SR,O[25]
ANL(APSFEL)	0.385	0.65ps	354	184	648	3.3	2.2	RF,S[40]
Italy(ELETTRA)	0.2-0.4	28	1000	150	2x19	10	4.2	SR,O[38]
Orsay(Super-ACO)	0.3-0.6	15ps	800	0.1	2x10	13	4.5	SR,O[26]
Osaka(FELI3)	0.3-0.7	5ps	155	60	67	4	1.4	RF,O[27]
Okazaki(UVSOR)	0.24	6ps	607	10	2x9	11	2	SR,O[28]
Tsukuba(NIJI-IV)	0.2-0.6	160ps	310	5	2x42	7.2	2	SR,O[29]
Duke(OK-4)	0.1947	1.6ps	800	35	2x33	10	0-4	SR,O[30]
DESY(TTF1)	0.109	0.5ps	233	300	492	2.73	1.17	RF,S[42]
PROPOSED ======	-------	-------	-------	-------	-------	-------	-------	-------
Florida(CREOL)	355	8μs	1.3	0.13	185	0.8	0.1	EA,O[31]
Netherlands(TEUFEL)	180	20ps	6	350	50	2.5	1	RF,O[32]
Rutgers(IRFEL)	140	25ps	38	1.4	50	20	1	MA,O[33]
Moscow(Lebedev)	100	20ps	30	0.25	35	3.2	0.8	MA,O[34]
Novosibirsk(RTM)	2-11	20ps	98	100	4x36	9	1.6	RF,O[35]
TJNAF(UVFEL)	0.16-1	0.2ps	160	270	72	3.3	1.3	RF,O[20]
Rocketdyne/Hawaii(FEL)	0.3-3	2ps	100	500	84	2.4	1.2	RF,O[36]
Harima(SUBARU)	0.2-10	26ps	1500	50	33,65	16,32	8	SR,O[37]
ANL(APSFEL)	0.12	1ps	440	150	864	3.3	3.1	RF,S[40]
BNL(DUVFEL)	0.1	6ps	230	1000	256	2.89	1.2	RF,A[39]
Frascati(COSA)	0.08	10ps	215	200	400	1.4	1	RF,O[41]
Duke(VUV)	0.01-1	1ps	1000	50	4x32	12	3	SR,O[43]
DESY(TTF2)	0.006	0.17ps	1000	2500	981	2.73	0.9	RF,S[44]
SLAC(LCLS)	0.00015	0.07ps	14350	3400	3328	3	3.7	RF,S[45]
DESY(TESLA)	0.0001	0.08ps	35000	5000	1200	5	4.2	RF,S[46]

RF - RF Linac Accelerator
SR - Electron Storage Ring
A - FEL Amplifier
SP - Smith-Purcell Oscillator
MA - Microtron Accelerator
EA - Electrostatic Accelerator
O - FEL Oscillator
S - SASE FEL

Table 2. The Short Wavelength FEL in 2000 (From [Ref. 26]).

The first column lists the operating optical wavelength l which is given by [Ref. 25]

$$l = \frac{l_0(1+K^2)}{2g^2} \tag{3.4}$$

where l_0 is the undulator wavelength, and K is the undulator parameter listed in the following column. The relativistic Doppler shift and Lorentz contraction due to the electron motion is included in the calculation of the radiated optical wavelength in Equation (3.4). This is called the resonance condition and occurs when the electron slips behind the optical wave by one optical wavelength as the electron traverses an undulator wavelength. From the simple relationship of (3.4), it is seen that an FEL can easily be designed to operate at a broad span of wavelengths, including wavelength regions where there are no powerful light sources. For example, no conventional laser operates in ultraviolet or an extreme ultraviolet range of the electromagnetic spectrum (300 to 30 nm) and no conventional laser operate in the far infrared (1mm to 20 μm) [Ref. 27].

The second column lists the normalized electron pulse length

$$s_z = \frac{\ell_e}{c}, \tag{3.5}$$

where ℓ_e is the electron pulse length and c the speed of light. From this column, it can clearly be seen that the majority of the FELs create micropulses and only a few work CW

The third column provides the electron beam energy E as it comes from the accelerator, ranging from a few MeVs up to 1 GeV in *ELETTRA* while the proposed electron beam energy is up to 30 GeV in the *TESLA* FEL facility. The next column shows the average peak current I ranging from a few milliamperes to 300A for the existing FELs and up to 5000A for the proposed FELs.

The fifth and sixth columns are parameters related to the undulator design. The number of undulator periods is N, and the undulator wavelength is

$$l_0 = \frac{L}{N} \tag{3.6}$$

where L is the undulator length. Note that in a few cases, in the N-column, there are multiple undulator sections, which are referred to in the FEL klystron undulator designs [Ref. 26]. The next column also depends on the design and is the undulator parameter

$$K = \frac{eBl_0}{2p\, m_e c^2} \tag{3.7}$$

where e is the electron charge magnitude and B is the rms undulator field strength. Take special note that the values of $K \sim 1$. For $K >> 1$, there will be radiation in many higher harmonics[Ref. 24], and for K<<1, FEL gain would be small.

The last column lists the accelerator type. Note that the majority are RF linear accelerators and oscillators, as in the experiment and simulations described in the chapters that follow.

B. FEL INTERACTION-PENDULUM EQUATION

In this thesis, as well as in most cases, Coulomb forces between the electrons are small because the beam energy is large. Relativistic electrons streaming in the z direction and interact with a helical undulator magnetic field,

$$\vec{B} = B_0 \left(\cos k_0 z, \sin k_0 z, 0\right) \tag{3.8}$$

where B is the magnetic field of the undulator and $k_0 = 2p / l_0$ is the undulator wavenumber. The electron Lorentz force equation is [28]

$$\frac{d(g\vec{b})}{dt} = -\frac{e}{m_e c}\left(\vec{E} + \vec{b} \times \vec{B}\right) \tag{3.9}$$

Initially, we find the electron trajectory through the undulator by assuming that there is no radiation $\vec{E} = 0$. The electron energy change is given by

$$\frac{dg}{dt} = -\frac{e}{m_e c}\vec{b} \cdot \vec{E} \tag{3.10}$$

which means that dg / dt is zero according Equation (3.10) for the $\vec{E} = 0$ case , so that g would be constant. The term $\vec{b} \times \vec{B}$ in Equation (3.9) is

$$\vec{b} \times \vec{B} = \hat{x}(-B_0 b_z \sin k_0 z) + \hat{y}(B_0 b_z \cos k_0 z) + \hat{z}(B_0 b_x \sin k_0 z - B_0 b_y \cos k_0 z) \tag{3.11}$$

Then, Equation (3.9) can be separated into components and becomes

$$\frac{db_x}{dt} = \frac{eB_0 b_z}{g m_e c} \sin k_0 z, \tag{3.12}$$

which by integration gives

$$b_x = -\frac{eB_0}{g m_e c^2 k_0} \cos k_0 z \tag{3.13}$$

since $dz/dt = b_z c$, and where it is assumed that the ejection of electrons is perfect and the constant of integration is zero. Substitute $k_0 = 2p / l_0$ Equation (3.13) becomes

$$b_x = -\frac{eB_0 l_0}{2pg m_e c^2} \cos k_0 z \tag{3.14}$$

Define the undulator parameter as $K = eB_0 l_0 / 2pg m_e c^2$ so that Equation (3.14) becomes

$$b_x = -\frac{K}{g} \cos k_0 z. \tag{3.15}$$

Similarly for the y-component, we have

$$b_y = -\frac{K}{g} (\sin k_0 z). \tag{3.16}$$

The vector addition of the components in Equations (3.15) and (3.16) gives the electron velocity in the transverse direction $\vec{b}_\perp = (b_x, b_y, 0)$. Thus,

$$\vec{b}_\perp = -\frac{K}{g} (\cos k_0 z, \sin k_0 z, 0) \tag{3.17}$$

Now that we have the electron trajectory, we add radiation to find the microscopic motion. Taking into account the radiation created in the undulator, consider a circularly polarized plane wave for the optical field of the form

$$\vec{E}_s = E(\cos y, -\sin y, 0), \tag{3.18}$$

$$\vec{B}_s = E(\sin y, \cos y, 0). \tag{3.19}$$

Here $y = kz - wt + j$, E is the electric and magnetic field amplitude in cgs units, $k = w/c$ is the optical wavenumber, and j is the optical phase.

With radiation included Equation (3.9) becomes

$$\frac{dg}{dt} = -\frac{e}{m_e c} E(b_x \cos y - b_y \sin y). \tag{3.20}$$

Substitution of Equations (3.15) and (3.16) into (3.20) yields

$$\dot{g} = \frac{eKE}{g m_e c} \cos(z + j), \tag{3.21}$$

where $\dot{g} = dg/dt$ and $z + j = y + k_0 z = (k + k_0)z - wt + j$. z is defined as an electron phase, which describes the electron position in the combined undulator and optical fields (k_0 and k terms). Note that in Equation (3.21), the rate of change in energy, $\dot{g}$, is proportional to the electric field E and the undulator parameter K, but inversely proportional to the energy of the electrons g. As the energy of the incoming electrons is increased, the coupling with the optical field is reduced.

Expanding Equation (3.2), the Lorentz factor reads

$$g^{-2} = 1 - b_z^2 - b_\perp^2, \tag{3.22}$$

and substituting Equation (3.17) in Equation (3.22) yields

$$g^{-2}(1 + K^2) = 1 - b_z^2. \tag{3.23}$$

Taking the time derivative on both sides of Equation (3.23) gives

$$-2g^{-3}\dot{g}(1 + K^2) = -2b_z \dot{b}_z \Rightarrow \frac{\dot{g}}{g} = \frac{g^2 b_z \dot{b}_z}{1 + K^2}. \tag{3.24}$$

Recall that the electron phase is

$$z = (k + k_0)z - wt, \tag{3.25}$$

and by differentiating Equation (3.25) twice gives

$$\dot{z} = \left[(k+k_0)\dot{z}\right] - w = \left[(k+k_0)b_z\right] - w, \tag{3.26}$$

$$\ddot{z} = (k+k_0)\dot{b}_z c \Rightarrow \dot{b}_z = \frac{\ddot{z}}{(k+k_0)c}, \tag{3.27}$$

and by inserting the result of $\dot{b}_z$ in Equation (3.24) we get

$$\frac{\dot{g}}{g} = \frac{g^2 b_z \ddot{z}}{(1+K^2)(k+k_0)c}. \tag{3.28}$$

For relativistic electron, $k >> k_0$ and $b_z \approx 1$, so that Equation (3.28) can be written as

$$\frac{\dot{g}}{g} = \frac{g^2 \ddot{z}}{(1+K^2)kc} = \frac{g^2 \ddot{z}}{(1+K^2)w} \tag{3.29}$$

The resonance condition of Equation (3.4), with l is replaced by $2\pi c/w$ can be written as

$$w = \frac{w_0 2g}{1+K^2}. \tag{3.30}$$

Substituting Equations (3.21) and (3.30) in Equation (3.29) and solving for $\ddot{z}$ gives

$$\ddot{z} = \frac{2w_0 eKE}{m_e c g^2}\cos(z + \phi). \tag{3.31}$$

Dimensionless parameters are introduced to make the model simpler and more physically meaningful. The dimensionless time $t \cong ct/L$ describes the electron and optical evolutions that take place as t ranges from $0 \to 1$. The time derivatives now are $(\dot{..}) = d(..)/dt$ instead of $(\dot{..}) = d(..)/dt$. The dimensionless optical complex field is defined as

$$a = |a| e^{i\phi} \tag{3.32}$$

where $|a| = 4\pi NeKLE/g^2 mc^2$ is the dimensionless optical field amplitude. Applying all the new dimensionless quantities, Equation (3.31) takes the form of a simple pendulum equation

$$\ddot{z} = |a|\cos(z + j). \tag{3.33}$$

Equation (3.33) governs the electron's microscopic phase dynamics relative to the optical field inside the undulator. Therefore, the complicated motion of the electrons is described by this simple and well-known pendulum equation. The positive or negative acceleration in Equation (3.33), is proportional to values of the cosine term and results in the bunching of the electrons within an optical wavelength. Consider a group of electrons uniformly distributed in phase. The electrons with phases in the range $-p/2 < z + j < p/2$ will gain energy and speed up, while the electrons in the range $p/2 < z + j < 3p/2$ will experience a loss in energy and slow down. As a result, the electrons have the tendency to bunch together near $z = p/2$. This bunching coupled with the wave equation contributes to a net energy transfer to the optical field.

The dimensionless field amplitude $|a|$ of Equation (3.33) determines the electron bunching rate along the undulator. If $|a| >> p$, the optical field is strong and the bunching occurs quickly. If $|a| << p$, the optical field is weak and the change in the electron phase velocity is small [Ref. 24].

The wave equation that drives the complex optical dimensionless field of Equation (3.32) can be put into the following simple form [Ref. 25]

$$\dot{a} = -j < e^{-iz} > \tag{3.34}$$

where the dimensionless electron beam current $j = 8N(epKL)^2 r / g^3 m_e c^2$, r is the actual electron beam density, and $\langle .. \rangle$ in the wave equation indicates an average over all the electrons. This average will be non-zero only when the electrons are bunched. The rate of change of the optical field is proportional to the dimensionless current j.

The pendulum Equation (3.33) and the wave Equation (3.34) are coupled together through the dimensionless current j. If $j \le 1$, the gain is low, and if $j >> 1$ the gain is high. Both the pendulum and wave equations, even in this simple form, are valid in high and low gain regimes, as well as in weak and strong optical fields.

C. PHASE SPACE ANALYSIS

The electron evolution and the optical wave are coupled accordingly in Equations (3.33) and (3.34). The phase-space evolution of sampled electrons is used to describe the motion of the electrons over an optical wavelength. Each electron is started with its initial conditions $z_0 = z(0)$ and $n_0 = n(0)$ at the beginning of the undulator $(t = 0)$. The phase velocity is given in dimensionless notation as

$$n = \frac{dz}{dt} = \dot{z} = L\left[(k + k_0)b_z - k\right]. \tag{3.35}$$

At resonance, $n = 0$, so solving (3.35) for b_z and using the resonance condition $l = l_0(1 + K^2)/2g^2$ and the approximation that $g >> 1$:

$$b_z = \frac{k}{k + k_0} \approx 1 - \frac{1 + K^2}{2g^2}. \tag{3.36}$$

Substituting b_z into Equation (3.35) yields

$$n = L\left[(k + k_0)(1 - \frac{1 + K^2}{2g^2}) - k\right] \approx -Lk\left(\frac{1 + K^2}{2g^2}\right), \tag{3.37}$$

using $k_0 << k$. Now differentiating Equation (3.37) with respect to g, substituting $L = N l_0$, and applying the resonance condition gain gives:

$$\Delta n = 4p N\left(\frac{\Delta g}{g}\right). \tag{3.38}$$

From Equation (3.38), it is clear that the change in phase velocity is related to the change in the electron energy. Figure 10 shows the phase space evolution for electrons at resonance and above resonance. In the first case, electrons are injected into the undulator with initial electron velocity $n_0 = 0$. They appear as yellow spots (evolution denoted by yellow going to red). Note that the electrons between $-p/2 < z < p/2$ increase their phase velocity by absorbing energy from the optical field. An equal number of electrons between $p/2 < z < 3p/2$ decelerate and transfer energy to the optical beam. Thus, the

net energy transfer is zero. On the top right of the figure, where the output of the optical gain $G(t)$ is located, it can be clearly seen that a resonant electron beam has no gain.

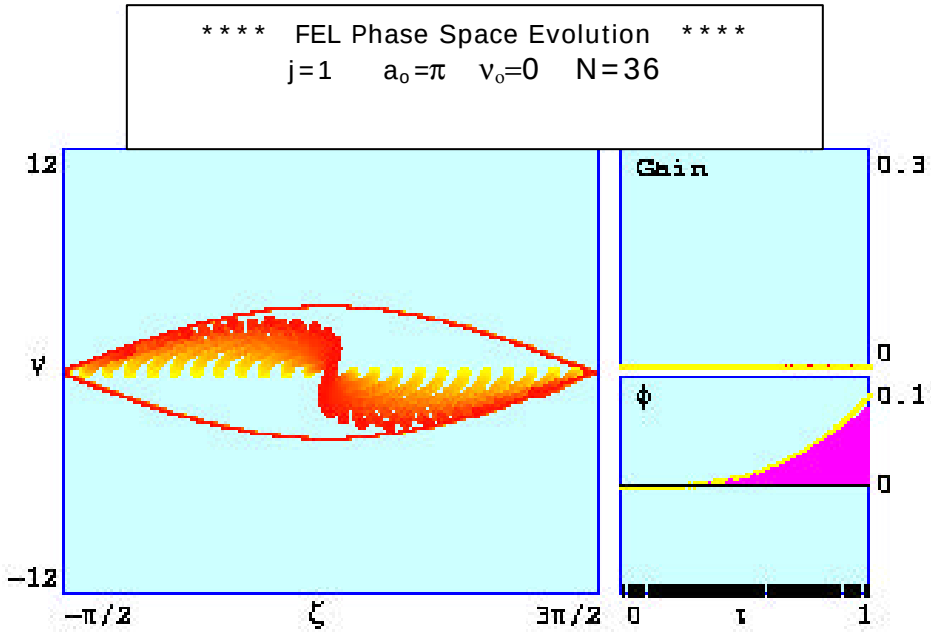

(a)

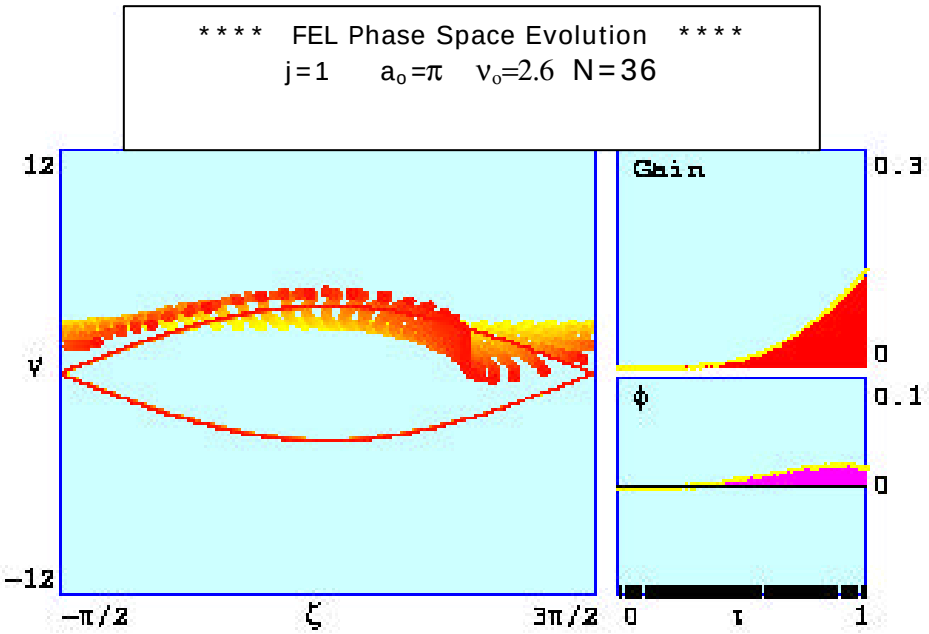

(b)

Figure 10. The Phase-Space Evolution at Resonance (a), at Optimum Initial Velocity (b).

On the other hand, the bunching that occurs near the relative phase $z + j = p/2$, drives the optical phase j in Equation (3.33). The optical phase $j(t)$ is plotted below the gain and it is relatively large, (~0.1).

Electrons injected slightly above resonance at $n_0 = 2.6$, are shown in the bottom part of Figure 10. In the phase space evolution for $t = 0 \rightarrow 1$ along the undulator, bunching near $z = p$ occurs. This bunching indicates that a significantly larger number of electrons transfer energy to the optical field and the gain is increased to $G = 12.5\%$.

The curve is shown in red in the same figure is called the "separatrix". It separates the closed and open orbits in phase space (phase-space paths) and connects unstable fixed points at $z = -p/2,\ 3p/2$ and $n = 0$. The separatrix points (z_s, n_s) are given by [Ref. 25]

$$n_s^2 = 2|a|[1 + \sin(z_s + j)]. \tag{3.39}$$

The peak-to-peak height of the separatrix is $4|a|^{1/2}$. Electrons outside the separatrix follow open orbits; those inside the separatrix are trapped in closed orbits.

D. GAIN

From the wave Equation (3.34), it is clear that if $j = 0$, then $\overset{\circ}{a} = 0$ and there is no gain. If the dimensionless current is small $j << p$, then a small change in the optical field amplitude occurs, and the gain is low since the electron phase velocity does not change much during the evolution through the undulator. Today, the majority of the operating FELs are low-gain, low-current FELs, and based on the following assumptions, it is possible to derive the weak field gain.

- Assume weak fields: $a << p$, $j = 0$
- Assume low gain: $\overset{\circ}{a} \approx 0 \Rightarrow a = a_0$, $\overset{\circ}{j} \approx 0$

With these assumptions, the pendulum equation can be solved analytically by expanding z and n in a power series.

The zero order expansion is

$$\begin{aligned} z^{(0)} &= z_0 + n_0 t \\ n^{(0)} &= n_0. \end{aligned} \tag{3.40}$$

To first order in a_0, where $a_0 = |a(0)|$, the pendulum equation gives

$$\begin{aligned} z^{(1)} &= -\frac{a_0}{n^2}\left[\cos(z_0 + n_0 t) - \cos z_0 + n_0 t \sin z_0\right] \\ n^{(1)} &= \left[\sin(z_0 + n_0 t) - \sin z_0\right]. \end{aligned} \tag{3.41}$$

In order to have net energy transfer from the electrons to the optical beam, we must satisfy $\langle n \rangle - n_0 \neq 0$, where $\langle n \rangle$ is the average phase velocity over all the electrons. The average of the $\langle n^{(1)} \rangle$ in Equation (3.41) is zero because the average of the sin function is $\langle \sin \rangle = 0$ which means that just as many electrons gain energy as lose energy. Therefore, second orders terms are needed to obtain non-zero gain, so that we find

$$n^{(2)} = \frac{a_0^2}{n_0^3}\left[-\frac{1}{4}\left(\cos(2z_0 + 2n_0 t) - \cos(2z_0)\right) + \cos(n_0 t) - 1 - n_0 t \sin(z_0)\cos(z_0 + n_0 t)\right] \tag{3.42}$$

The average of the second order term is

$$\langle n^{(2)} \rangle = n_0 + \frac{a_0^2}{n_0^3}\left[\cos(n_0 t) - 1 + \frac{1}{2} n_0 t \sin(n_0 t)\right] \tag{3.43}$$

The above dynamics of the electron position is related to the energy transfer, with the relation $\Delta n = 4\pi N(\Delta g / g)$. Both sides are averaged to find the average change in the electron beam energy

$$\Delta \bar{g}\, mc^2 = g\, mc^2 \frac{\left(\langle n \rangle - n_0\right)}{4\pi N}. \tag{3.44}$$

Energy conservation is used to calculate the gain $G(t)$. Gain is defined as the ratio of the energy transfer from electrons, Equation (3.44), divided by radiation beam energy in cgs units, $2E_s^2 dV / 8\pi$, in a volume dV, where E_s is the electric optical field. The filling factor F is defined as the ratio of the electron beam area divided by the optical mode area

$$F = \left(\frac{r_b}{w_0} \right)^2, \tag{3.45}$$

where r_b is the electron beam radius and w_0 is the optical beam radius at the waist. The number of electrons in a volume dV is given by $\rho F dV$, where ρ is the electron density. Thus the gain at time t is given by

$$G(t) = -\frac{(\rho F dV) g mc^2 (\langle \eta \rangle - \eta_0) / 4\pi N}{2E^2 dV / 8\pi}. \tag{3.46}$$

In the exchange of the energy, the second order contribution of Equation (3.43) is used. Also, the definition of dimensionless current $j = 8N(e\pi KL)^2 \rho F / \gamma^3 mc^2$ is used. Using these relations in to Equation (3.46) yields

$$G(t) = \frac{j}{\eta_0^3} \{ 2 - 2\cos(\eta_0 t) - \eta_0 t \sin(\eta_0 t) \}. \tag{3.47}$$

From the above equation, the strong relationship between the gain of the optical field and the initial phase velocity η_0 can be seen.

Figure 11 shows the output of simulations in the weak-field, weak-current regime. The final gain $G(t = 1)$, as well as the final optical phase shift $\psi(t = 1)$ versus the initial phase velocity, η_0, is plotted.

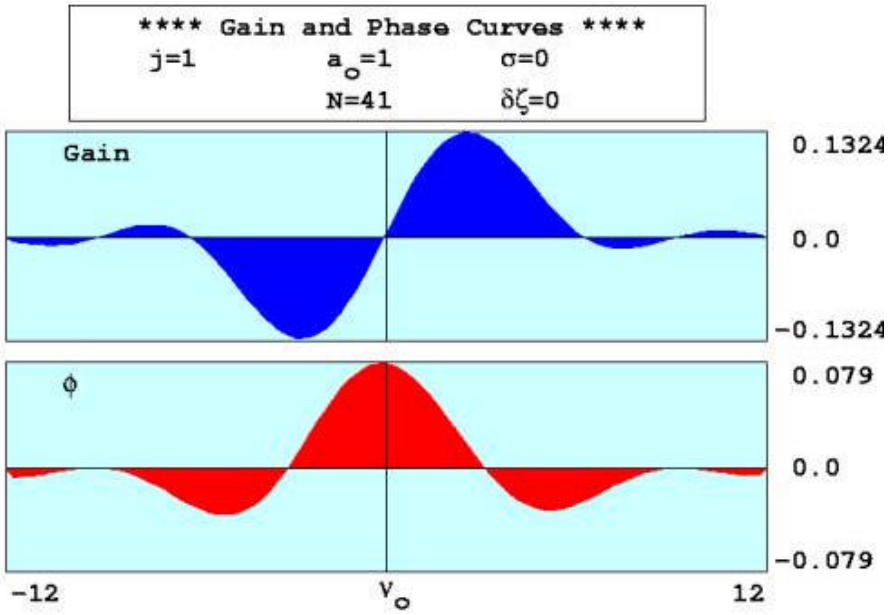

Figure 11. Weak-Field, Low-Current Gain $G(n_0)$ and Optical Phase Shift $j(n_0)$ Spectra.

The simulation result is in total agreement with the analytic results of Equation (3.47). The initial phase velocity, which is a function of the electron beam energy (recall that $\Delta g / g = \Delta n_0 / 4pN$), determines the final gain. At the resonance condition, $(n_0 = 0)$, the gain is reduced to zero. On the other hand, the optical field drives the optical phase shift, with a peak value of $\Delta j = 0.8 j$. There is a peak gain of $G = 0.13 j$ when the initial velocity is $n_0 = 2.6$ and the optical phase shift is reduced to $\Delta j = 0.02$. As the gain spectrum is anti-symmetric around $n_0 = 0$, there are losses for negative initial phase velocities $(n_0 < 0)$ and accordingly, the maximum absorption occurs at $n_0 = -2.6$.

E. SHORT PULSES

From the last column of Table 1 it is clear that the majority of FELs use radio-frequency accelerators (RF). Electrons are ejected in short pulses from an electron-gun with a frequency f and are accelerated. The separation distance between the pulses is c/f. Thus, for $f = 750$ MHz, the pulses are separated by 40 cm. The pulse length that is currently used for FEL oscillators is often picoseconds and is comparable to the slippage distance Nl, where N is the number of undulator periods.

In the picosecond scale, the short-pulses effect the FEL interaction. As electron "buckets" enter an undulator length L, short optical pulses are produced due to spontaneous emission. These optical pulses bounce between the mirrors of the resonator separated by distance *S*. The optical pulse after a time $2S/c$ arrives back at the beginning of the undulator. If the incoming electron buckets enter the undulator at the same time and coincide with the optical pulse, exact synchronism occurs. The displacement between optical and electron pulses is called desynchronism, *d*, and in exact synchronism $d = 0$. As the optical pulses enter the undulator simultaneously with electron pulses,gain development is delayed. This effect is called *lethargy* [Ref. 25]. The electron pulses travel slightly slower than the optical pulses. The electron pulses fall behind and preferentially amplify the trailing part of the optical pulse; so the centroid of the optical pulse travels slower than the speed of light. After each pass, the optical pulse falls farther behind the electron pulse and consequently, after some passes, the power starts to decay.

Figure 12 shows the short pulse evolution at exact synchronism, $d = 0$. The lower left window shows the electron pulse position for $t = 0$ and $t = 1$. The electron pulse shape is parabolic and has the form $j(z) = j\left(1 - 2z^2 / s_z^{\,2}\right)$ for $j(z) > 0$ and is zero otherwise. The normalized pulse length is s_z and the dimensionless current $j = 5$. The middle-left window corresponds to the field evolution, $|a(z,n)|$, over the passes n=500 passes. Note that the optical field shifts to the left as the centroid of the light pulse travels slower than the speed of light *c*. The final optical pulse shape $|a(z)|$ is shown in the upper left window. In the specific simulation output, the optical field and the power decay accordingly after $n \approx 150$ passes.

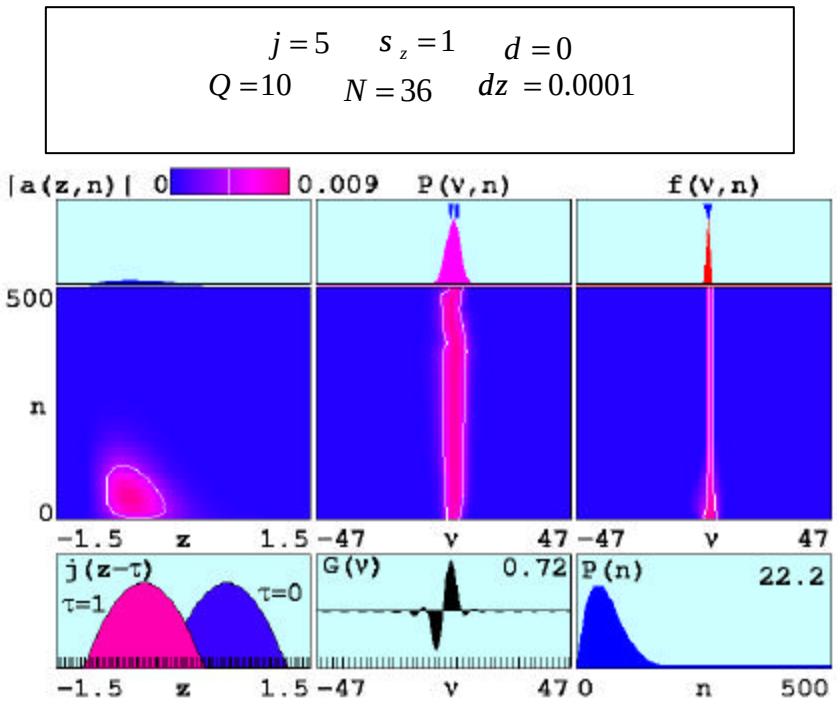

Figure 12. Short Pulse Evolution at Exact Synchronism.

The middle lower window represents the weak field spectrum $G(n_0)$ and is plotted for reference. The window above that shows the evolution of the optical power spectrum $P(n,n)$ over $n = 500$ passes. The final power spectrum $P(n)$ is in the top-middle window. The pointed tick-mark at the top indicates the initial optical wavelength derived from the resonance condition. The thicker mark indicates the center of the final spectrum.

The lower-right window shows the dimensionless optical power $P(n)$ at the end of each pass. The middle right window shows the evolution of each of the electron energy spectrum $f(n,n)$ over $n = 500$ passes. The upper-right window shows the final electron spectrum after n = 500 passes. Again, the pointed tick-mark shows the initial phase velocity of the electron beam at resonance. The thicker tick-mark indicates the position of the final average electron phase velocity $\langle \Delta n \rangle$.

In exact synchronism, the steady state power is reduced to zero. The slower speed of the light pulse centroid is overcome by reducing the path inside the resonator by ΔS. To do so, piezoelectric crystals move the mirrors slightly and $d = -2\Delta S / N l$. Figure 13 shows, an FEL has the same design characteristics as the FEL in Figure 12, but with $d = 0.06$ instead of $d = 0$.

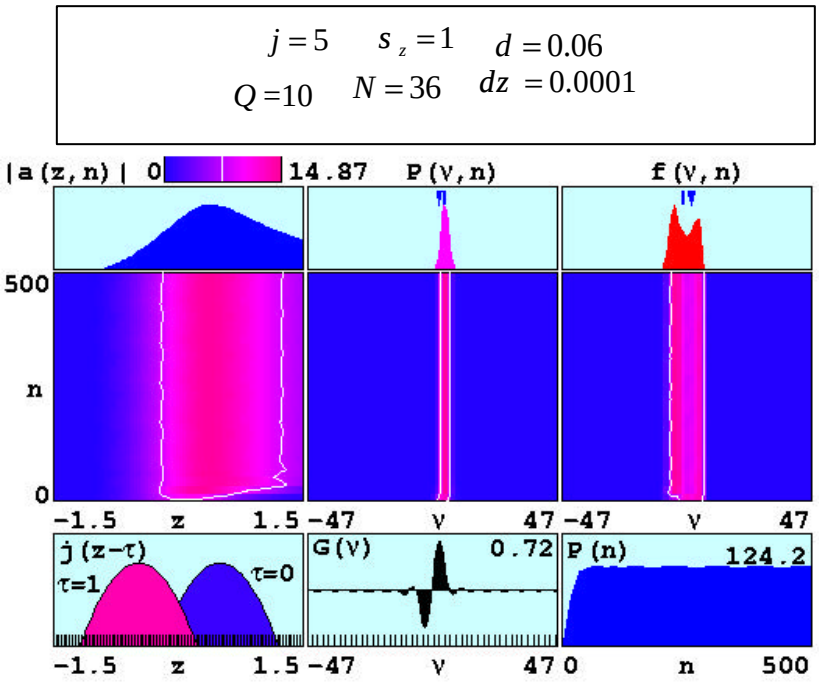

Figure 13. Short Pulse Evolution at Relative Large Desynchronism.

The introduction of a small amount of desynchronism $d = 0.06$ allows the FEL to produce a steady state power after $n = 50$ passes.

As will be seen in the chapters to follow, desynchronism is important to the characteristics of pulse evolution. By increasing desynchronism *d*, less power is obtained but the FEL becomes more stable. The final optical pulse is longer than the electron pulse and as a result, the power spectrum is narrow. Increasing the desynchronism too much will cause the electro-optical pulses to not overlap sufficiently and consequently, the FEL will not operate.

THIS PAGE INTENTIONALLY LEFT BLANK

IV. SIMULATIONS OF THE 100KW TJNAF FEL

A. INTRODUCTION

The Thomas Jefferson National Accelerator Facility (TJNAF) FEL has demonstrated 2 kW output power of tunable infrared radiation [Ref. 29]. This is the highest average power level from an FEL in the world and was achieved with a design leading towards the further development of get higher power. A schematic representation of the system is shown in Figure 14.

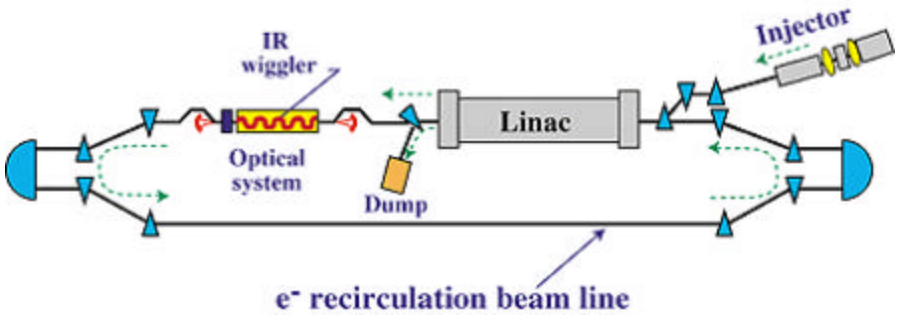

Figure 14. TJNAF FEL "From [Ref. 30]."

In order to operate at higher output power levels, the TJNAF FEL utilizes electron beam recirculation. Energy recirculation or "energy recovery" is the process by which the same electron beam is returned to the accelerator. After the interaction inside the wiggler, the recirculated electrons arrive back at the linear accelerator "Linac" 180 degrees out of phase so that their energy is converted back into RF power used to accelerate subsequent electrons.

The energy spread that a specific system can recirculate is limited. The limitations come from the induced RF phase shift upon arrival at the wiggler, which is equal to optical desynchronism. The change in desynchronism alters the FEL gain and the laser output power. Consequently, these optical power changes result in a change in the energy of the recirculating electron beam, which can potentially lead to additional electron beam loss on apertures and a phase shift of the decelerated beam. The power variations, the phase shifts and the beam loss can change the beam-induced voltage in the accelarator cavities. The process can be refered to as a "beam loading instability" [Ref. 31]. If the rf

control system does not possess sufficient gain and bandwidth, the whole recirculating FEL becomes unstable.

Another constraint on recirculation occurs in bending magnets of static ble magnetic fields are used for the 180 degrees turns. The momentum of the electrons spread resulting from the FEL interaction leads to a range of bending radii that can drive some of the electron beam into the wall of the vacuum pipes and cause the FEL to cease lasing. Overall , there are many benefits to recirculation, such as the enhancement to the wall-plug efficiency and reduction of harmful radiation in the beam dump, so recirculation is desirable.

In the course of developing megawatt power levels, which is required for a weapon, it is advisable to proceed step by step. Studies at TJNAF have indicated that the system can be upgraded to operate at an increased power of 100 kW. This upgrade has been proposed with a projected demonstration scheduled for 2005 [Ref. 11].

To support this goal, simulations were conducted to determine gain, steady-state extraction efficiency and the induced energy spread. The input data for simulations were design parameters chosen by the TJNAF scientists [Ref. 32]. To achieve 100 kW average power, the kinetic energy of the electron beam increased to $E_e = 210\,\text{MeV}$ and the pulse repetition rate to $\Omega = 750\,\text{MHz}$. The average electron beam power is given by

$$P_e = E_e \hat{I} \ell_e \Omega / c \tag{4.1}$$

where $\hat{I} = 270\,\text{A}$ is the peak current in the electron micropulse, $\ell_e = 0.1\,\text{mm}$ is the electron micropulse length and c is the speed of light. The average electron beam power then calculated as $P_e = 14\,\text{MW}$. Therefore an output power of 100 kW requires an extraction efficiency of approximately $h = 0.7\%$.

The undulator period is $l_0 = 8\,\text{cm}$ over $N = 36$ periods with an rms undulator parameter of $K = 1.7$. Table 1 summarizes the experimental parameters.

Electron energy	E_e = 210 MeV
Peak electron pulse current	$\hat{I}$ = 270 Amp
Electron pulse length	ℓ_e = 0.1 mm
Number of undulator periods	N = 36
Undulator wavelength	l_o = 8 cm
Undulator length	L = 288 cm
Resonator length	S = 36 m
Optical wavelength	l = 1 mm
Step-Taper	$\Delta = 0, \pm p, \pm 2p$

Table 3. TJNAF 100kW FEL Parameters.

In the simulations presented here, different undulator designs were investigated to access their possible advantageous effects on the FEL interactions. The conventional undulator possesses a periodic magnetic field and wavelength, but a linearly tapered undulator gradually changes the undulator parameter K as shown in Figure 15 by modifying the gap between the undulator magnets along the undulator length. The field can either increase or decrease along the undulator length.

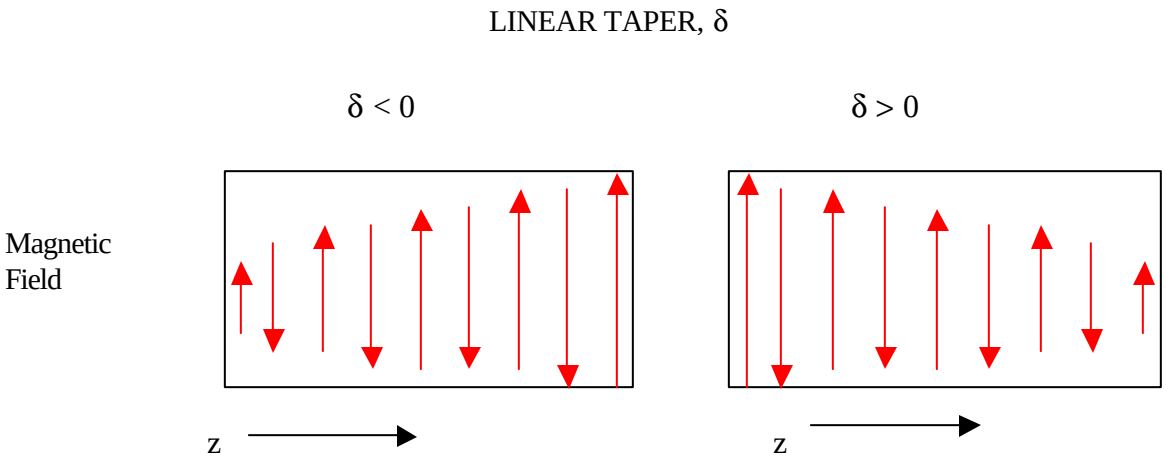

Figure 15. Schematic for a Linear Taper Wiggler.

A step-tapered undulator abruptly changes the value of the field and K halfway through the undulator as Figure 16 shows. The stepped field can decrease or increase as shown.

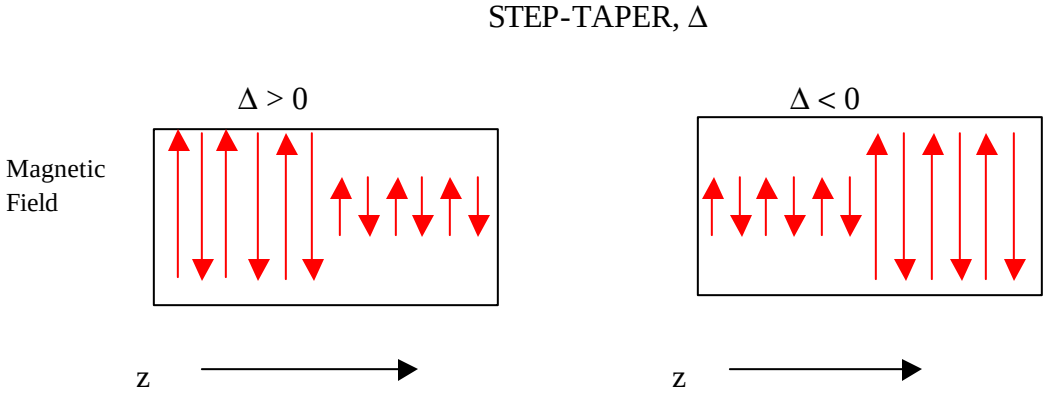

Figure 16. Schematic for a Step-Taper Wiggler.

The resulting FEL interaction in a tapered undulator [Ref. 25], [Ref. 33]-[Ref. 37] is described by the modified pendulum equation

$$\dot{n} = \ddot{z} = d + q\left(t - \frac{1}{2}\right)\Delta + |a|\cos(z + j) \tag{4.2}$$

$$\text{where } q(z) = \begin{cases} 0 \text{ for } z < 0 \\ 1 \text{ for } z > 0 \end{cases} \text{ is the step function,}$$

$z = (k + k_0)z - wt$ is the electron phase, $k = 2p / l$ is the optical wavenumber, $k_0 = 2p / l_0$, is the undulator wavenumber, $w = kc$ is the optical frequency, n is the electron phase velocity, j is the optical phase,

$$a = |a|e^{ij} \tag{4.3}$$

a is the complex dimensionless optical field, $|a| = 2p\, NeKL|E|/g^2 mc^2$, and,

$$d = -4p\, NK^2\left(\frac{dK}{K}\right)(1 + K^2) \tag{4.4}$$

where d is the phase acceleration caused by the linear tapering of the undulator, dK/K is the fraction change in the undulator parameter along the whole undulator length,

$$\Delta = -4p\,NK^2\left(\frac{\Delta K}{K}\right)(1+K^2) \tag{4.5}$$

is the step-taper along the undulator at

$$t = \frac{z}{N\,l_o} = \frac{1}{2}, \tag{4.6}$$

and $\Delta K/K$ is the step change in the undulator parameter at $t = 1/2$.

B. WEAK FIELD GAIN

The 100 kW TJNAF FEL is described by the dimensionless current $j = 5$, the electron pulse length

$$s_z = \frac{\ell_e}{\mathrm{N}\,l} = 3 \tag{4.7}$$

and the resonator cavity quality factor of $Q = 4.2$. To study the FEL gain, a weak optical field is used so that the dimensionless field is $|a| < p$ The desynchronism *d* is given by

$$d = -\frac{\Delta S}{N\,l} \tag{4.8}$$

and measures the shortening of the resonator cavity length by ΔS compared to the slippage distance $N\,l$. The desynchronism between the optical pulse and the electron pulse was varied from $d = 0$ to $d = 0.3$. The FEL gain results from many simulations at different values of desynchronism d with a step-tapered undulator are plotted in Figure 17.

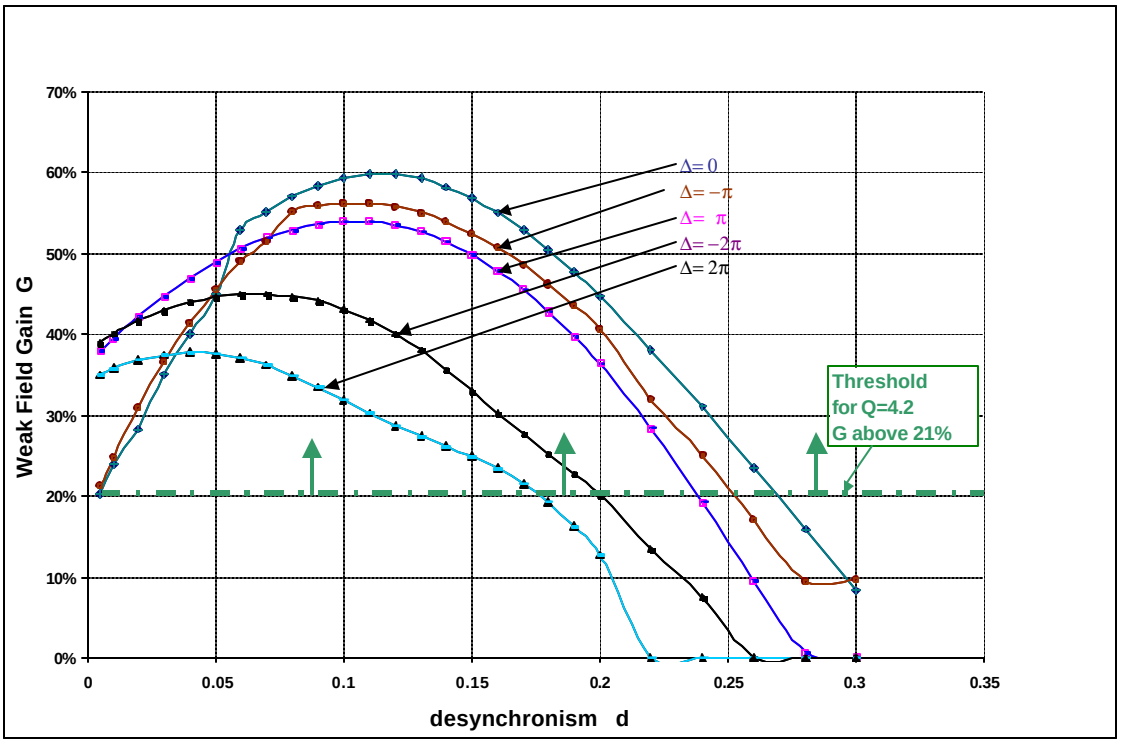

Figure 17. Weak Field Gain G versus Desynchronism d.

For the conventional non-tapered case, $(\Delta = 0)$, it can be seen that the highest gain is 60%. At small and large values of desynchronism, the gain decreases for all the undulators away from peak values around $d = 0.1$. The gain for small step-tapers of $\Delta = \pm p$ is only slightly reduced from the conventional case. Larger step-tapers $\Delta = \pm 2p$ cause a significant reduction in gain down to around 40%, peaking at the lower values of $d \sim 0.05$. Also, the FEL still works above the threshold losses $(Q = 4.2)$ for larger values of $d < 0.2$.

Figure 18 shows the gain spectrum for an FEL with an inverse taper rate of $\Delta = -2p$ over $N = 36$ periods with a current density of $j = 6$. These parameters are descriptive of the proposed TJNAF 100 kW FEL.

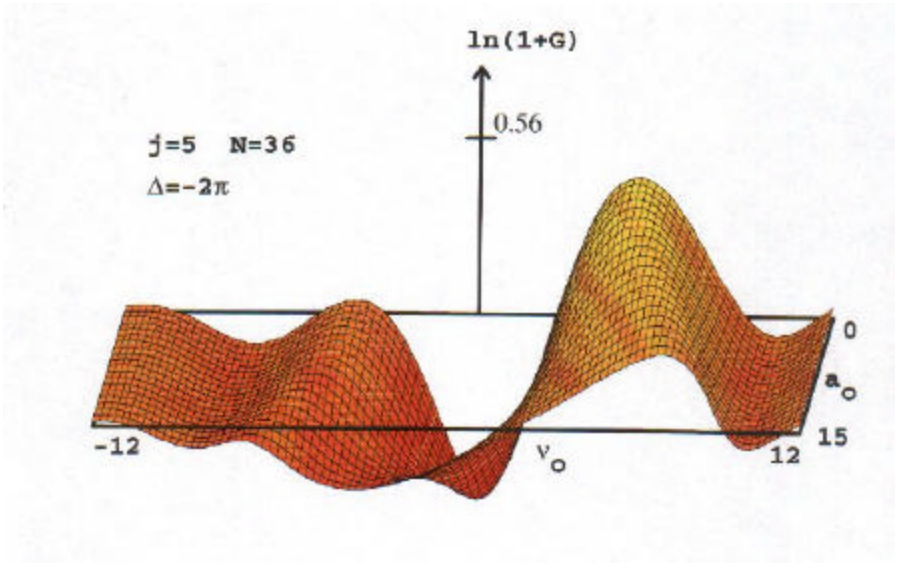

Figure 18. Gain vs. n_o for Inverse Step Taper $\Delta = -2\pi$.

For a negative step taper, the gain decreases in strong fields but still remains significant. Also, increasing the optical field a_o results in a small increase in the phase velocity for peak gain.

In the electron pendulum phase-space, determined by Equation (4.2), the negative step taper $\Delta = -2p$ FEL shows 1% efficiency with 3.8% induced energy spread. Figure 19 shows a simulation in a strong optical field where electron bunching is evident in phase space evolution.

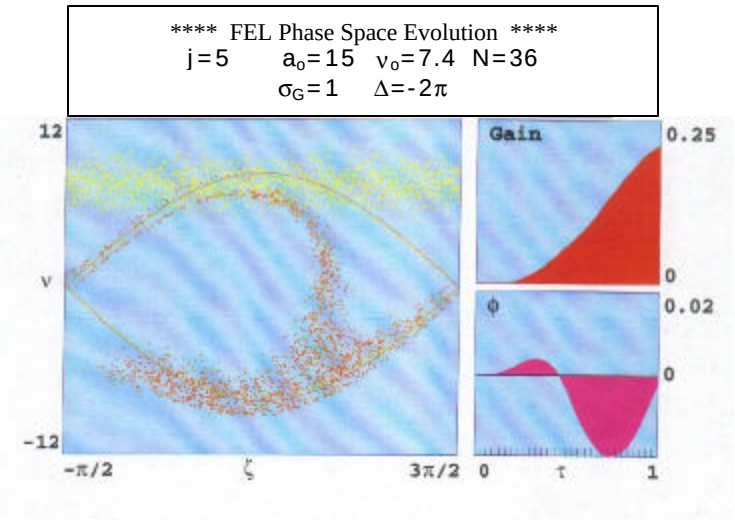

Figure 19. Phase Space for Step-Taper $\Delta = -2\pi$ Undulator.

As can be seen in the figure the electrons start at initial phase velocity $n_0 = 7.4$ with a random spread in phase velocities of width $s_n = 1$. The light colored dots show the phase space position at the beginning of the undulator, while the darker colored dots show the position at the end. At phase position $z \approx p$, the electrons are bunched, amplify the optical field and lead in a gain G ~23%. The optical phase at this position is small f ~0.02 and further reduced to f ~0 at the end of the undulator.

C. STEADY STATE EXTRACTION EFFICIENCY

For a conventional undulator with no taper, the desynchronism was varied from $d = 0.005$ up to 0.3 to study the pulse slippage effects. The best results for desynchronism were $d = 0.04$, with an efficiency of $h = 0.08$ above the requirement for 100kW. At that value of desynchronism, the induced energy spread was $\Delta g / g = \Delta n / 4p N = 3\%$, which is well below the 15% limit for recirculation. Figure 20 shows that slight increases in desynchronism to $d > 0.06$ makes the efficiency marginal $(h < 0.7\%)$ for reaching 100 kW.

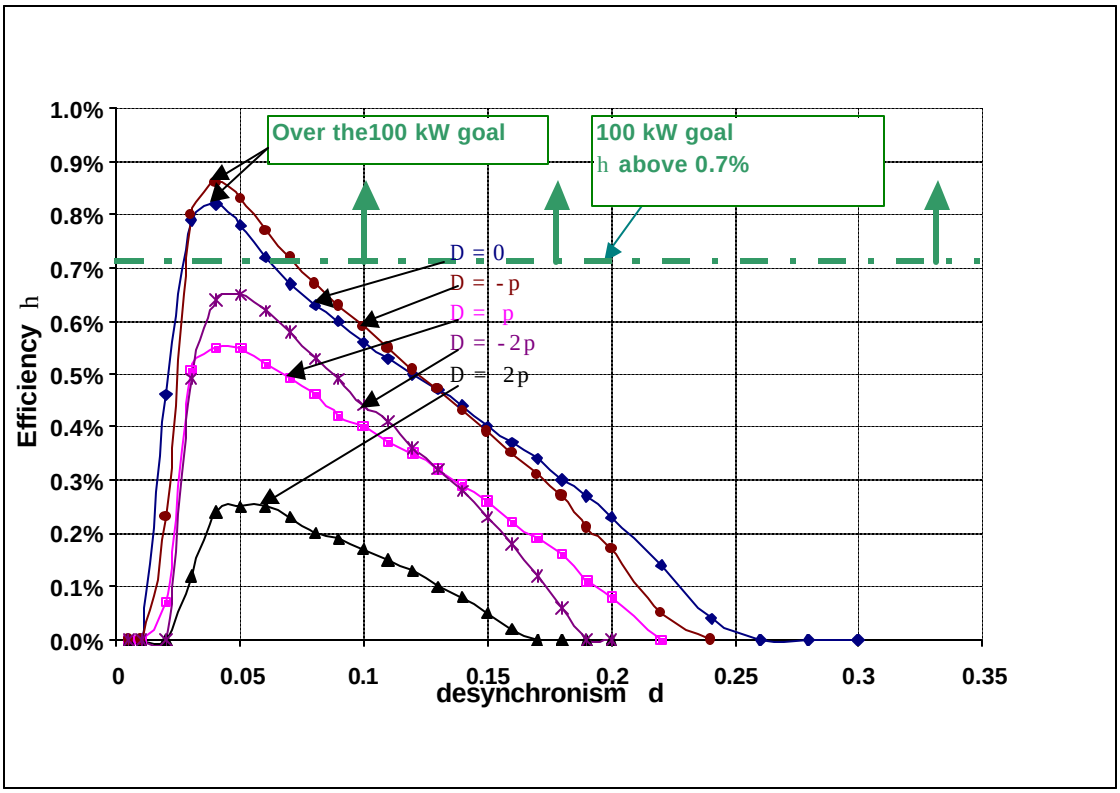

Figure 20. Efficiency η Versus Desynchronism d.

Additionally for a step-taper undulator, the results of longitudinal multimode simulations are shown in the same figure. Again, the efficiency is plotted versus desynchronism d for different values of Δ. For the same value of $d = 0.04$, a negative step-taper $\Delta = -p$ once again demonstrated the best results, and the efficiency increased to $\sim 0.9\%$.

Figure 21 presents a high power example for the $\Delta = -p$ case with a desynchronism value of $d = 0.04$.

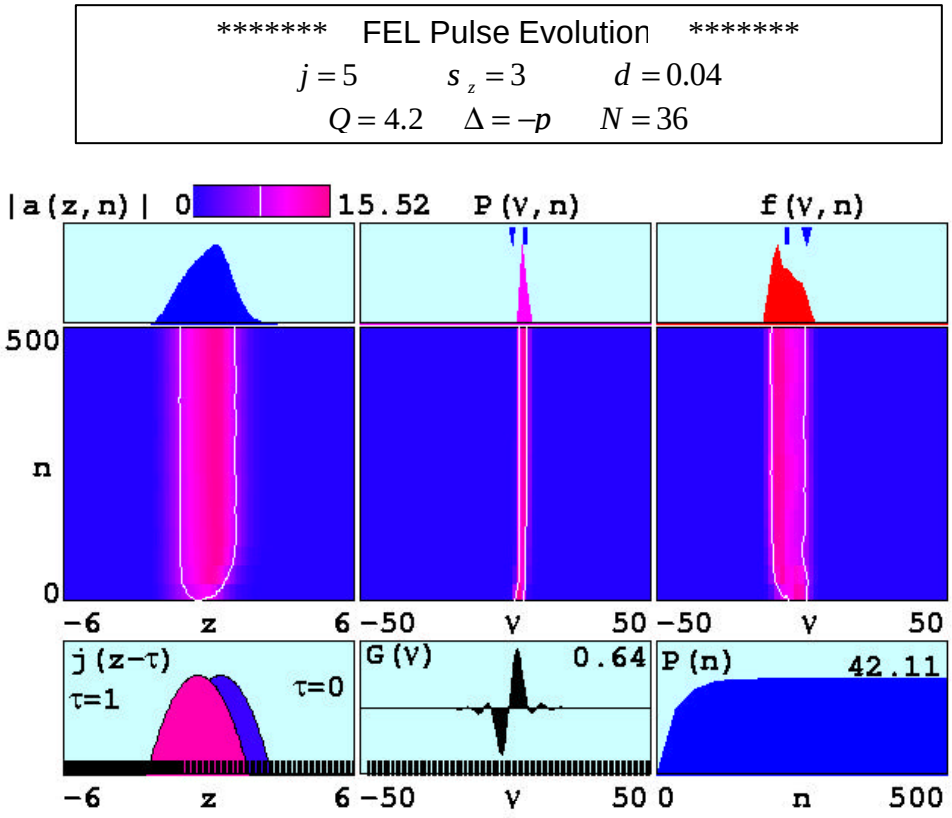

Figure 21. Power Simulation for Inverse Step-taper Undulator.

The efficiency for this case is $h = 0.86\%$, which corresponds to an output power of 116 kW. The induced electron energy spread is only $\Delta g / g = 2.4\%$, which is within the 15% specification for recirculation. The power reaches a steady state in less than $n = 50$ passes and remains steady throughout the whole experiment. The good behavior of the power evolution P(n) is indicated at the bottom right window (steady state power after

500 passes). Larger values of tapering $\Delta < -2p$, and desynchronism $d > 0.06$ did not work.

With both the linear and step taper, a slight increase in efficiency over the conventional undulator was observed for the small negative taper.

The induced energy spread did not change much with any undulator design as is shown in Figure 22.

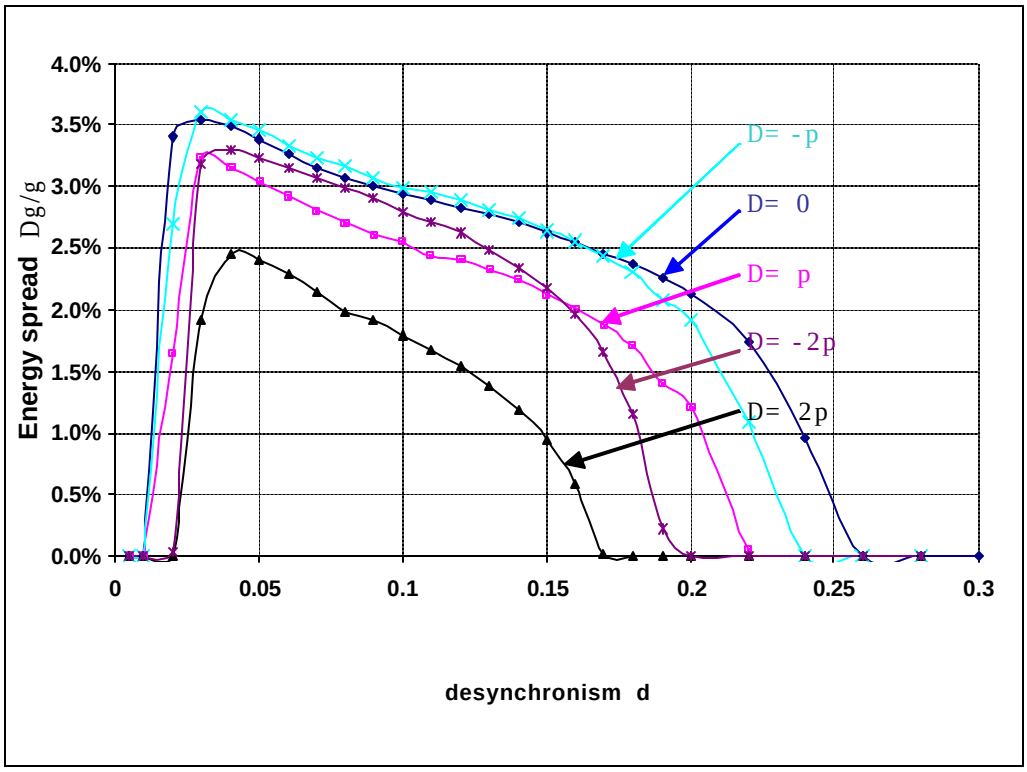

Figure 22. Energy Spread Δγ/γ versus Desynchronism d for Step-Taper with Q=4.2. Lower Power Reduces Energy Spread for all Undulator Designs.

The maximum values of the induced electron energy spread were found in the region with maximum efficiency. Taper rates $\Delta = 0, -p$ result in energy spreads of $\Delta g / g = 3.5\%$ and 3.7% respectively. These values were the largest found for all undulator designs and were far less than the maximum allowable limit for safe beam recirculation around 15%. For this reason, the quality factor Q was increased from 4.2 to 10. The new resonator cavity will only have 10% losses per pass. Also, larger efficiency and induced electron energy spreads were examined.

D. HIGHER Q EXPERIMENTS

The purpose of these simulations was to explore regions beyond the design parameters and find the optimum undulator design. The quality factor Q was increased from 4.2 to 10 while the rest of the input data remained similar. Such experiments have been conducted at TJNAF and are described in the following chapter.

1. Step-Taper Wiggler

One of the proposed designs was to make use of the step-tapered wiggler. For this design the extraction efficiency and the induced electron energy spread were explored.

a. Extraction Efficiency

In the simulations, the step-taper rates $|\Delta|$ were applied from $0 \rightarrow 4p$. In Figure 23 the curves show the result of simulations with a quality factor of $Q = 10$.

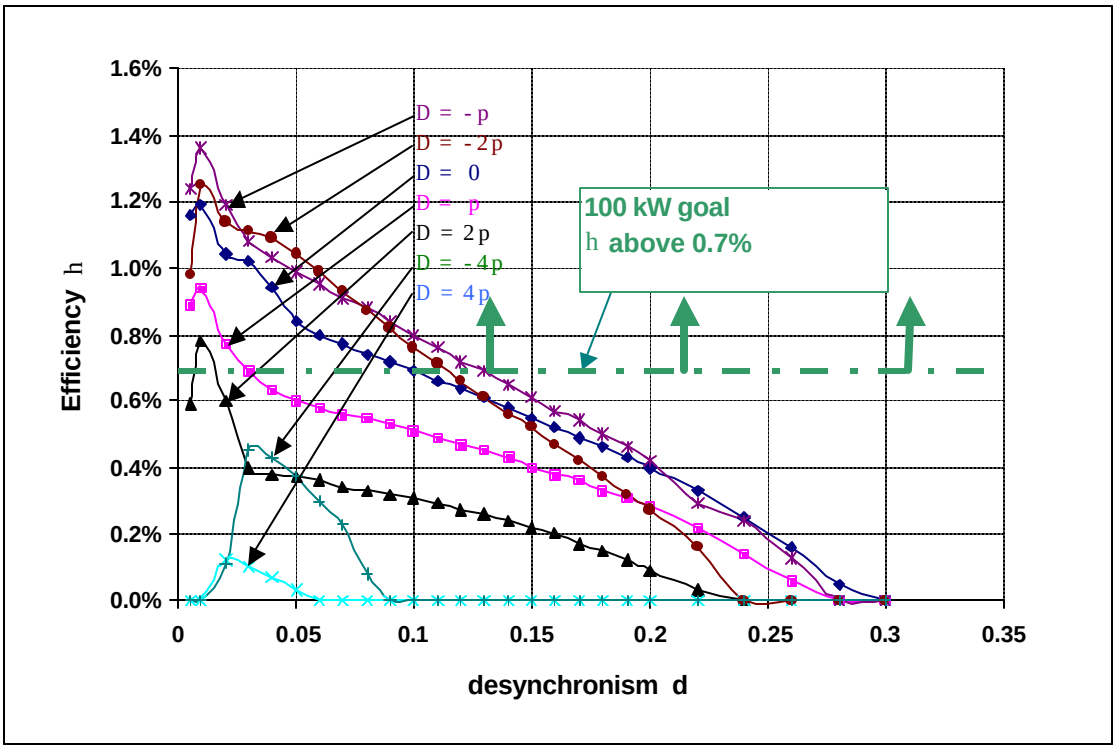

Figure 23. Efficiency η versus Desynchronism d for Step-Taper, and Higher Q=10. Power Above 100 kW for a Larger Range of Tapers $\Delta = 0, \pm\pi, \pm 2\pi$.

In this case, the extraction efficiency for some values of D and d exceeds 1%. In this case of $\Delta = -p$, the efficiency increased from 0.9% to 1.4%. For all values of

$\Delta = \pm 4p$ and for a desynchronism of $d > 1.2$, the FEL failed to exceed the efficiency limit. Compared to the case of $Q = 4.2$, there is a larger range of desynchronism in which the FEL operates above the extraction efficiency requirement of $h > 0.7\%$. Moreover, other taper rates, such as $\Delta = +p, \pm 2p$, were able to produce output power of exceeding 100 kW. This result is significant, because it was not confined to a small region of parameters. See Figure 7 for $Q = 4.2$. More acceptable taper rates of D and a larger d lead to more stable, and therefore, more desirable systems. The simulation output for the optimum inverse taper of $\Delta = -p$ at $d = 0.03$ is presented in Figure 24.

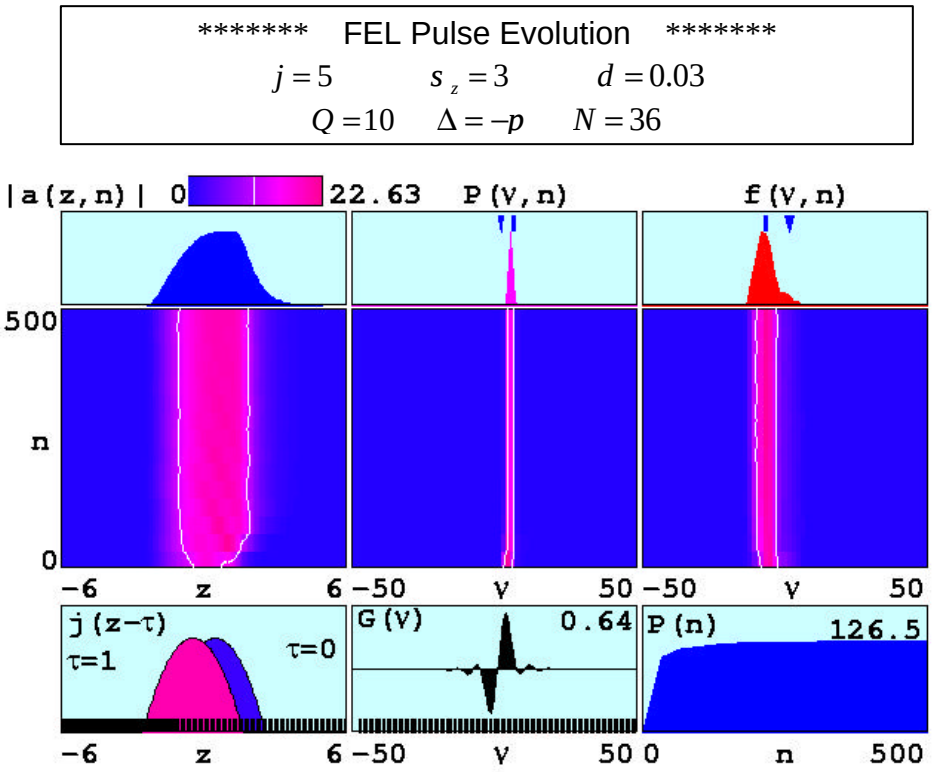

Figure 24. Power Simulation for $\Delta = -\pi, Q = 10$.

In this figure, the steady state power is evident and the induced energy spread is limited. The efficiency $h = 13.6\%$ results in an output power of 190 kW which is almost double that of the objective. Also, for this power, the induced energy spread $\Delta g / g = 4.3\%$ is again within a safe limit.

b. Induced Energy Spread

The new design in the cavity $Q = 10$ increased the induced electron energy spread significantly. Nevertheless, as Figure 25 shows, it is still below the maximum acceptable limit of 15% and our design can recirculate the electron beam.

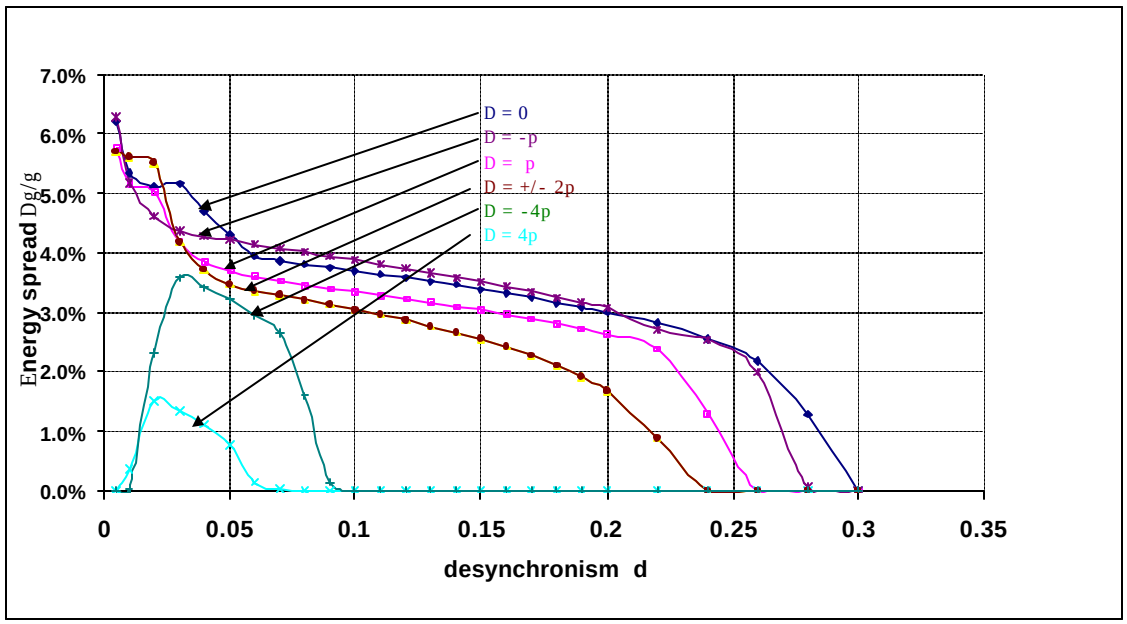

Figure 25. Energy Spread $\Delta\gamma/\gamma$ for Step-Taper, $Q = 10$.

2. Linear Taper Wiggler

A linearly tapered wiggler gradually changes the undulator parameter K by modifying the gap between the undulator magnets. A schematic representation was given in Figure 15.

a. Extraction Efficiency

In simulations, the linear taper rate d applied was varied over the values $d = 0, \pm p, \pm 2p, \pm 4p$, and corresponds to $\Delta K / K = \pm 0.9\%, \pm 1.9\%, \pm 3.8\%$. Recall from equation (4.4) that $d = -4p\, NK^2 (\Delta K / K)(1 + K^2)$.

The operating rate of desynchronism d between the optical and electron pulses was varied from $0 \rightarrow 0.3$. Figure 26 shows the extraction efficiency as a function of desynchronism and the taper phase acceleration d.

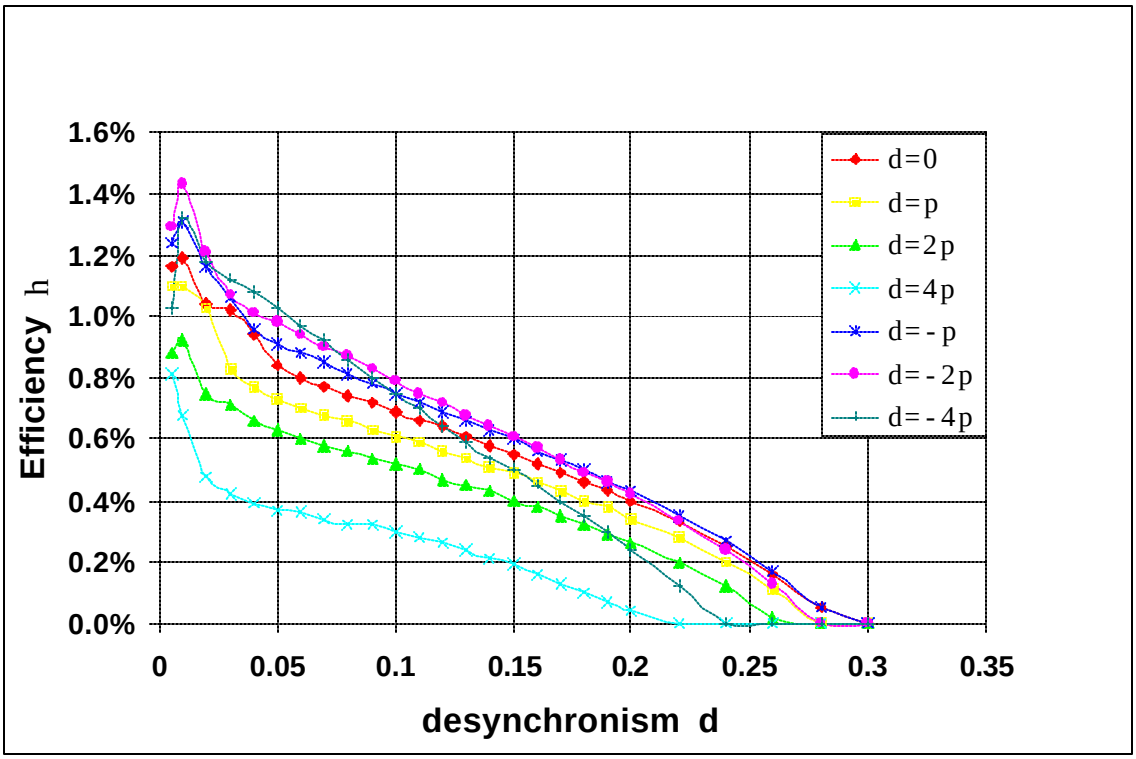

Figure 26. Efficiency η versus Desynchronism d for Linear Taper with Q=10. Power Above 100 kW for a Larger Range of Tapers.

Once again, it is found that the negative taper results in maximum efficiency. For the linear taper rate $d = -2p$, there was a maximum efficiency of h ~1.4% at $d = 0.01$. For the untapered undulator $d = 0$, there was a maximum efficiency of $h = 1.2\%$ at the same value of d. Other undulators with negative taper rates of $d = -p, -4p$ reach $h = 1.3\%$, which is better than the zero tapered undulator. Note that 1.0% efficiency is easily achieved from almost all taper rate values of d with the exception of positive tapers $d = 2p, 4p$. For these taper values, $h = 0.9\%$ and $h = 0.8\%$ occurred respectively. These values of extraction efficiency are the smallest, but still result in an output average power of more than 100 kW.

b. Induced Energy Spread

A smaller exhaust energy spread allows the intense electron beam to recirculate without damaging components. Figure 27 shows the final induced energy spread produced by seven different designs.

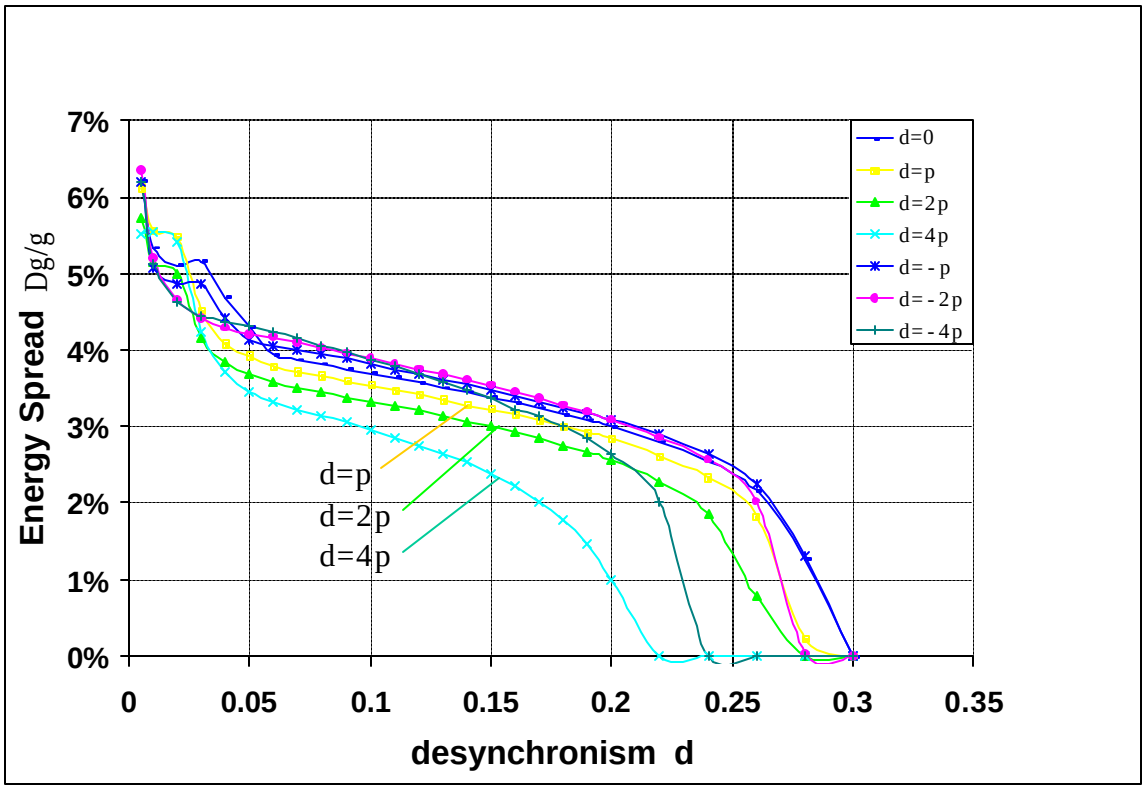

Figure 27. Energy Spread $\Delta g / g$ for Linear Taper, $Q = 10$.

The inverse taper undulator for $d = -2p$ has a peak energy spread of $\Delta g / g = 6.3\%$ occurring at $d = 0.01$. All the values of all taper rates, including the latter value, produce an energy spread below the maximum tolerable limit. An increase in desynchronism in order to reduce the electron beam energy spread is not necessary. Note that a positive linear taper produces the smallest energy spread compared to all other designs. In small values of desynchronism, all the taper rate values are almost comparable. However, after $d = 0.04$, the values that occur from the positive taper are significantly smaller.

E. CONCLUSIONS

The best results of 100 kW simulations for various designs and a quality factor of $Q = 4.2$ are summarized below in Table 4.

$Q = 4.2$, STEP TAPER DESIGN				
Step-Taper D	Desynchronism d	Efficiency $h(\%)$	Induced energy spread Dg/g (%)	Output Power P (kW)
0	0.04	0.82	3.5	115
π	0.04	0.55	3.2	77
2π	0.05	0.25	2.4	35
$-\pi$	0.04	0.86	~3.5	120
-2π	0.05	0.64	3.2	90

Table 4. Results of TJNAF 100 kW Step-Taper Undulator, for $Q = 4.2$.

Step-taper wigglers were explored and compared with conventional wigglers. For the given TJNAF 100kW FEL parameters, the inverse taper undulator $\Delta = -p$ achieved the highest final power at a desynchronism of $d = 0.04$. The output power produced was $P \sim 120$ kW which is above the 100 kW objective. The conventional untapered undulator, ($d = 0$), produced a final power of $P = 115$ kW, which again was above the objective at the same desynchronism value. In both cases, the induced electron energy spread $\Delta g / g \sim 3.5\%$ was smaller than the maximum allowable limit of 15% and did not limit the operational range of the FEL.

The small values of $\Delta g / g$ allowed for the possibility to explore a design with 10% losses ($Q = 10$) in an optical cavity. The high $Q = 10$ factor was chosen in such a way as to increase the efficiency of the system, while maintaining the induced energy spread well below the 15% engineering limit. The results related with Q, this design and the step-taper design are summarized in Table 5.

$Q = 10$, STEP TAPER DESIGN				
Step-Taper D	Desynchronism d	Efficiency $h(\%)$	Induced energy spread $Dg/g(\%)$	Output Power P (kW)
0	0.01	1.19	5.3	167
π	0.01	0.94	5.1	132
2π	0.01	0.78	5.6	109
4π	0.02	0.12	1.5	17
$-\pi$	0.01	1.36	5.1	190
-2π	0.01	1.25	5.3	175
-4π	0.03	0.45	3.5	63

Table 5. Results for Step-Taper, $Q = 10$ Design.

The best result for all the above cases was a taper rate of $\Delta = -p$ and occurred at desynchronism $d = 0.01$ with an output power of $P = 190$ kW. Moreover, all the designs, except $\Delta = \pm 4p$, operated above the threshold and are capable of producing an output power of at least 100 kW. The linear taper results are summarized in Table 6.

$Q = 10$, LINEAR TAPER DESIGN				
Linear Taper d	Desynchronism d	Efficiency $h(\%)$	Induced energy spread $Dg/g(\%)$	Output Power P (kW)
0	0.01	1.19	5.3	167
π	0.01	1.1	5.5	154
2π	0.01	0.92	5.1	129
4π	0.01	0.68	5.5	95
$-\pi$	0.01	1.31	5	183
-2π	0.01	1.43	5.2	200
-4π	0.01	1.32	5.1	185

Table 6. Linear Taper, $Q = 10$ Design.

The linear taper seems to be a very promising design. All taper rates, except for $d = 4p$, achieved 100 kW. For $d = -2p$ at a desynchronism of $d = 0.01$, the output power $P = 200\,\text{kW}$ was double the objective. From the table, the superiority of the inverse taper is clear. This kind of taper results in a large efficiency while the induced electron spread is comparable to other designs, and sufficiently lower than the 15% limit for safe recirculation.

The common behavior for all forms of taper rates is a reduction in extraction efficiency and the energy spread for a slight increase in desynchronism.

This work was presented at the 23rd International FEL Conference in Darmstadt, Germany and has been accepted for publication in Nuclear Instruments and Methods in Physics Research.

V. THE TJNAF TAPERED WIGGLER EXPERIMENT

A. INTRODUCTION

Using the Thomas Jefferson National Accelerator Facility (TJNAF) free-electron laser, experiments have been conducted which study its operation as a function of various taper rates and desynchronism values [Ref. 38]. The kinetic energy of the electron beam was $E_e = 34.5$ MeV, the optical wavelength was $l = 6\,\mu$m, the electron pulse duration was 0.5 ps (pulse length $\ell_e = 150\,\mu$m), and the peak current was $\hat{I} = 50\,$A. The purpose of the simulations presented here is to compare experiment with theory, and, by using a wider range of parameters than allowed by experiment, to extract more physical meaning from the results.

B. PARAMETERS AND SIMULATIONS METHODS

The simulations used the same parameters as TJNAF, described by dimensionless current density $j = 10$, normalized electron pulse length $s_z = \mathrm{N}l = 1$ and undulator parameter $K = 0.98$ (rms). Table 7 summarizes the experimental parameters and Table 8 the corresponding dimensionless parameters that are used in the simulations. The desynchronism between the optical pulse and the electron pulse was varied from $d = 0$ up to the highest value of d which produced power corresponding to an efficiency $h >$ 0.01%. As an example, the maximum desynchronism for the conventional non-tapered case $(d = 0)$ is $d = 0.4$. Not only were taper values for which we had experimental results explored, i.e. $d = 0$, $10p$, $-7p$, but values well beyond these were also explored. By using a wider range of values of linear taper, it was possible to plot the operating width of the desynchronism curve versus linear taper. The efficiency h and the induced energy spread $\Delta g / g$ are determined as functions of desynchronism d and taper acceleration d.

TJNAF EXPERIMENTAL PARAMETERS	
Electron Energy	$g\,mc^2$ =34.5 Mev
Undulator Length	L= 1.1 m
Undulator Periods	N= 41
Undulator Wavelength	l_o =2.7 cm
Peak Undulator Magnetic Field	B =5.5 kG
Peak Current	$\hat{I} = 50$ A
Taper Phase Acceleration	(d/p) = -7, 0, 10
Cavity Losses	Q =50

Table 7. Parameters used in the Experiment

DIMENSIONLESS SIMULATION PARAMETERS	
Current density	j =10
Electron Pulse width	s_z =1
Undulator Parameter	K= 0.98
Desynchronism	$d = 0 \rightarrow 0.4$
Taper Rate	$(d/p) = 0, \pm 3, \pm 6, \pm 7, \pm 8, \pm 9, \pm 10, \pm 12, \pm 14, \pm 16, \pm 18, \pm 20, \pm 22, \pm 24$

Table 8. Parameters used in the Simulations

C. UNTAPERED UNDULATOR

For an untapered undulator, the desynchronism was varied from $d = 0.002$ up to 0.4 in order to study pulse slippage effects. It was found that for desynchronism $d = 0.02$, the efficiency was $h = 0.04$. However, at this value the power P(n) is not steady, as shown in Figure 28 and the power oscillations are caused by the trapped-particle instability resulting from strong optical fields [Ref. 25].

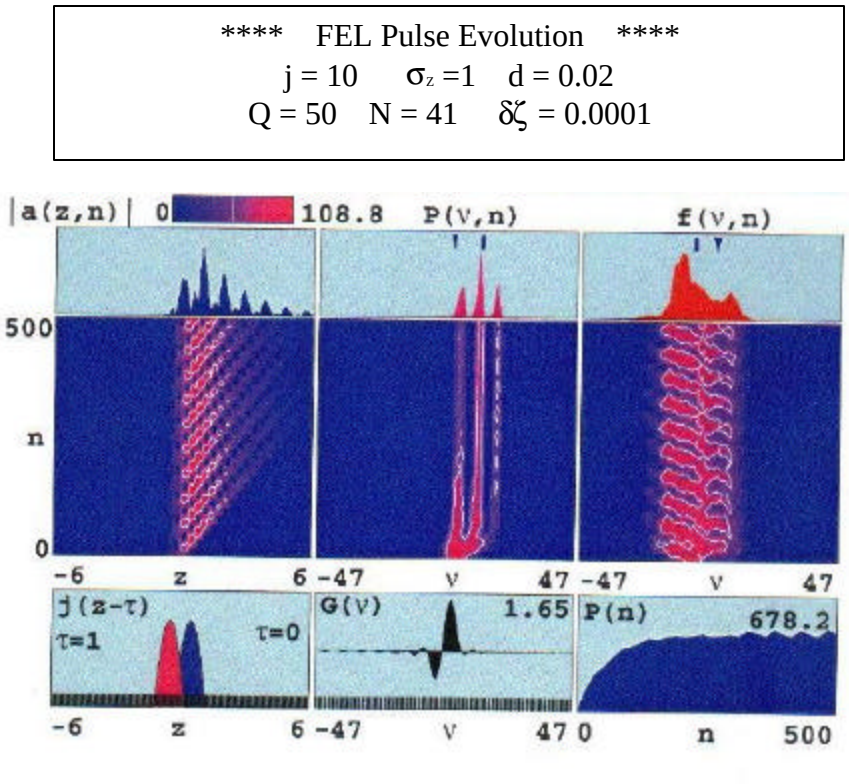

Figure 28. Trapped Particle Instability.

In the upper left window the final optical pulse shape after $n = 500$ passes is shown. There, short optical pulses, modulated with sharp spikes, create two sidebands in the optical power spectrum P(v,n) shown in the upper-middle plot. In the upper right window, the electron spectrum f(v,n) shows the large induced spread in phase velocities $\Delta n = 44$, which is not desirable for recirculation of the electron beam. The corresponding induced energy spread

$$\frac{\Delta g}{g} = \frac{\Delta n}{4p N} = \frac{44}{4p N} = 9\% \qquad (5.1)$$

Steady-state power without the trapped-particle instability or limit-cycle behavior [Ref. 39] is shown in Figure 29 for larger desynchronism of $d \geq 0.15$. Note the narrow electron distribution and the absence of sidebands in the power. Also note that the power evolution P(n) (bottom right) has no oscillations.

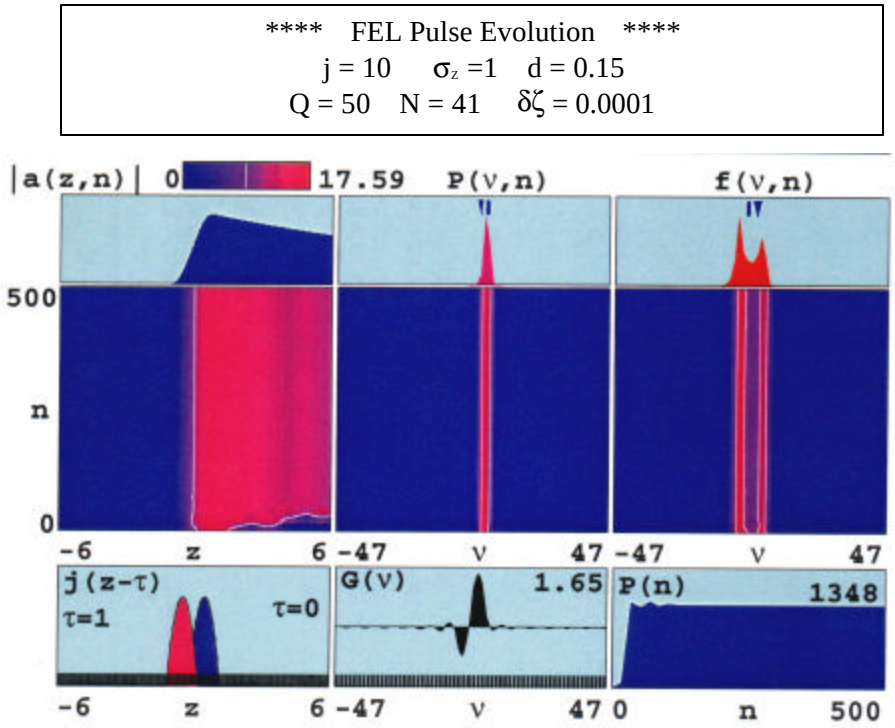

Figure 29. Steady State Power for Conventional Undulator.

D. GAIN SPECTRUM

The dimensionless electron phase velocity n. is the meeting point between simulations and experiments and in dimensionless notation is given by

$$n = 2p\mathrm{N}\left[1 - \frac{\left(1+\mathrm{K}^2\right)}{2g^2 l}\, l_o\right], \qquad (5.2)$$

where $\mathrm{N} = 41$ is the number of undulator periods and g is the relativistic Lorentz factor. Single mode simulations are used to find the optimum initial phase velocity n_o for maximum gain.

Figure 30 presents a plot of n_o as a function of the tapering rate d. The relation for peak gain $n_o = 2.4 - d/2$ is presented with the red circles and is valid in weak fields and moderate taper. Taper rates $d > 10p$ and strong fields $|a_o| > p$ change this relation.

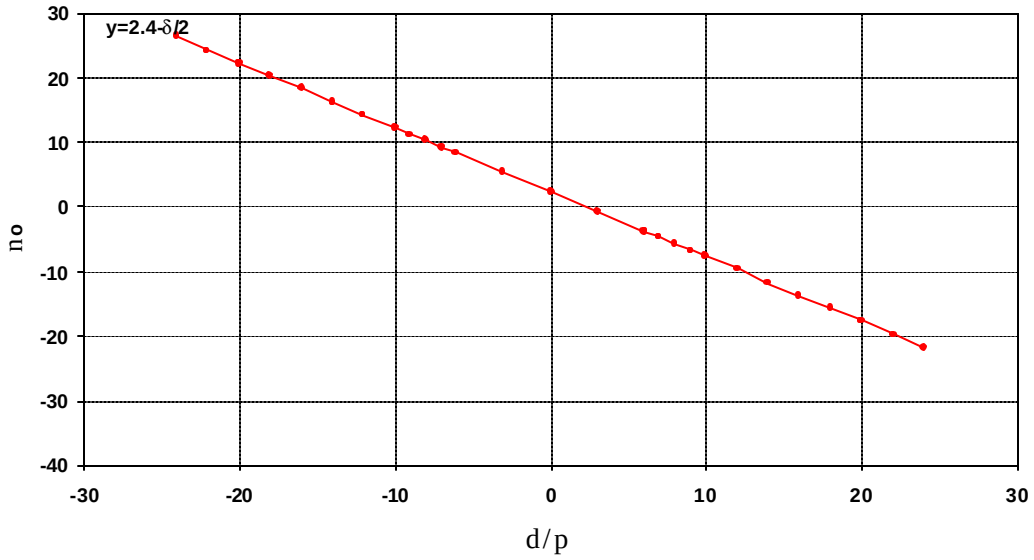

Figure 30. Plot of Phase Velocity versus Tapering Rate.

Figure 31 presents the peak gain as a function of taper by using the optimum initial phase velocity n_o of Figure 5. Is required for all tapering rates $-24p \le d \le 24p$, we have gain G that exceeds the resonator losses. The optical cavity losses, used in the experiment, were for $Q = 50$ so that, gain $G > 2\%$ is required for operation. The minimum gain, after introducing taper was $G = 7\%$, and was met for $d = 24p$.

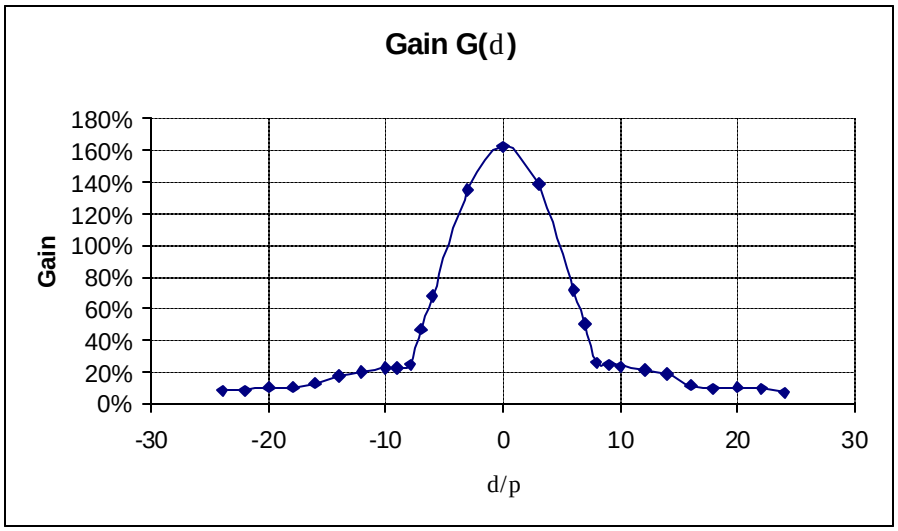

Figure 31. Peak Gain versus Taper Rate.

The G(δ) curve is almost symmetric in d with peak value at $d = 0$ where the gain is $G = 160\%$. As the magnitude of d increases, the peak gain decreases and for $d = \pm 24p$ reduces to $G \sim 8\%$. There is only a 1% difference in gain at the ends of the curve where negative taper results in slightly more gain.

Figure 32 (a) shows single mode gain plotted as a function of the initial optical field a_o and the initial electron phase velocity n_o. For $d = 0$, weak fields ($a_o < \pi$) and current j=10, the maximum gain is $G \approx 160\%$ and occurs at $v_o = 2.4$. Figure 32 (b) shows that the application of modest positive taper rate $(d > 0)$ makes the peak gain decrease and shift to the left in v_o. Figure 32 (c) shows similar results for the inverse taper $d < 0$ but shifts to a reduced peak gain to the right in v_o. For both positive and inverse tapers, it can be seen that gain is not symmetric around the resonance $(n_0 = 0)$ and for large values of optical field strength a_o, there is a distortion in the shape of the curve. Mention that positive taper has one gain peak in strong fields while negative taper has two, nearly equal, gain peaks in strong fields.

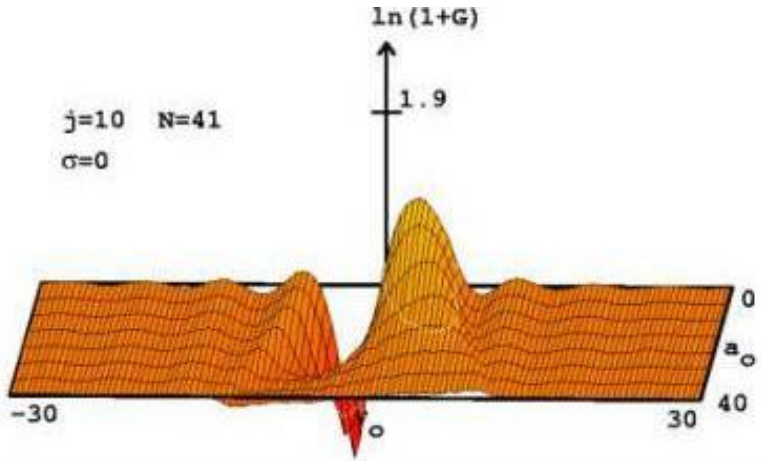

(a)

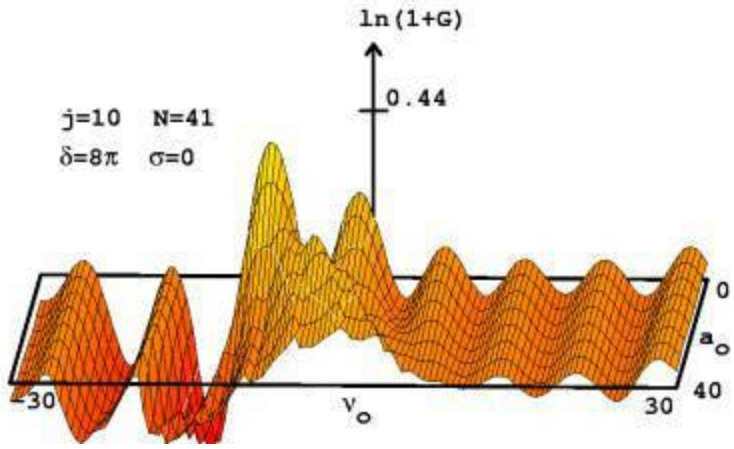

(b)

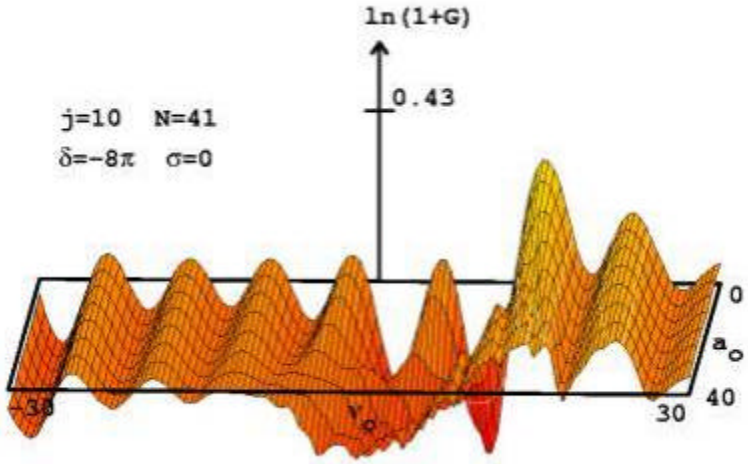

(c)

Figure 32. $G(\nu_0, a_0)$ for Zero taper (a), $\delta = 8\pi$ (b), $\delta = -8\pi$ (c).

E. STEADY STATE POWER

In our multi-mode simulations, the following values of linear taper were used:

$$d = \pm 3p, \pm 6p, \pm 7p, \pm 8p, \pm 9p, \pm 10p, \pm 12p, \pm 14p, \pm 16p, \pm 18p, \pm 20p, \pm 22p, \pm 24p.$$

Figure 33 summarizes the results of multimode simulations and plots the efficiency h for positive taper. The untapered undulator reaches its maximum efficiency $h = 4\%$ at $d = 0.002$. As the taper rate increases the efficiency decreases. For $d = 9p$, the efficiency is 50% smaller and peaks at $d = 0.006$. For $d = 14p$, the efficiency diminishes significantly to $h = 0.8\%$ at $d = 0.006$. After $d = 14p$, the peaks in the efficiency curves stay at lower values of desynchronism. Sidebands are formed due to the trapped-particle instability and the efficiency is enhanced up to 2% for $d = 16p$ at $d = 0.002$. Finally for larger taper rates $d = 24p$, the efficiency drops to only 1% at $d = 0.002$.

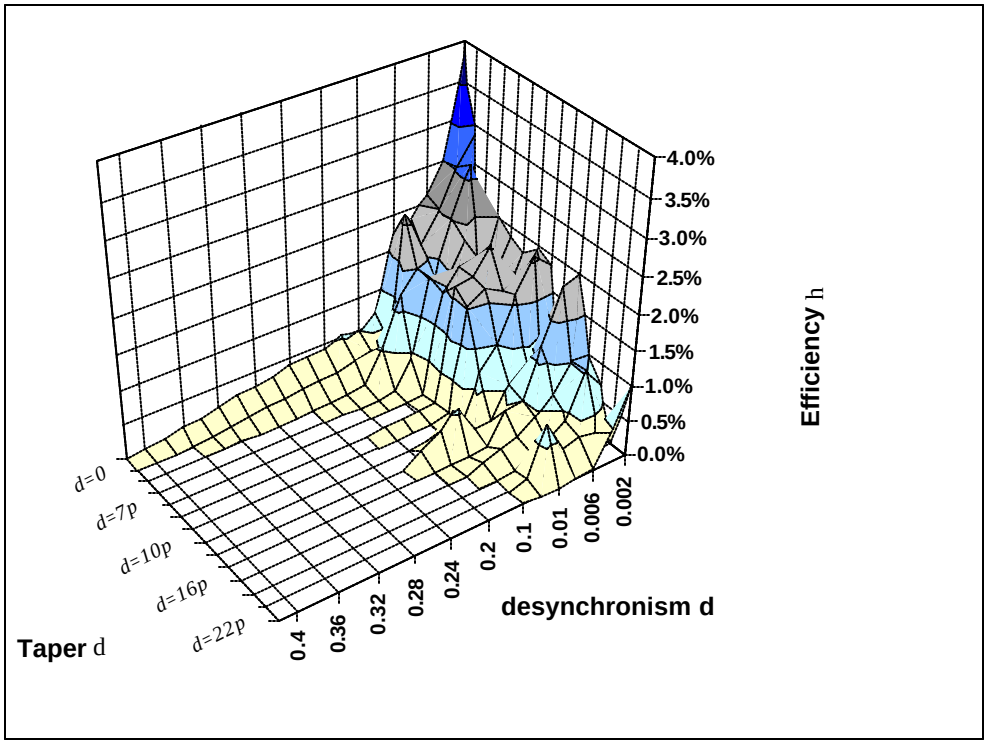

Figure 33. Efficiency $\eta(d,d)$ for Positive Taper.

In Figure 34 the efficiency is plotted as a function of desynchronism d for negative taper rates. As the taper rate increases from $d = 0 \rightarrow -3p$, the efficiency decreases from $4\% \rightarrow 2.6\%$. The peak of the efficiency curve continues to stay at small values of desynchronism.

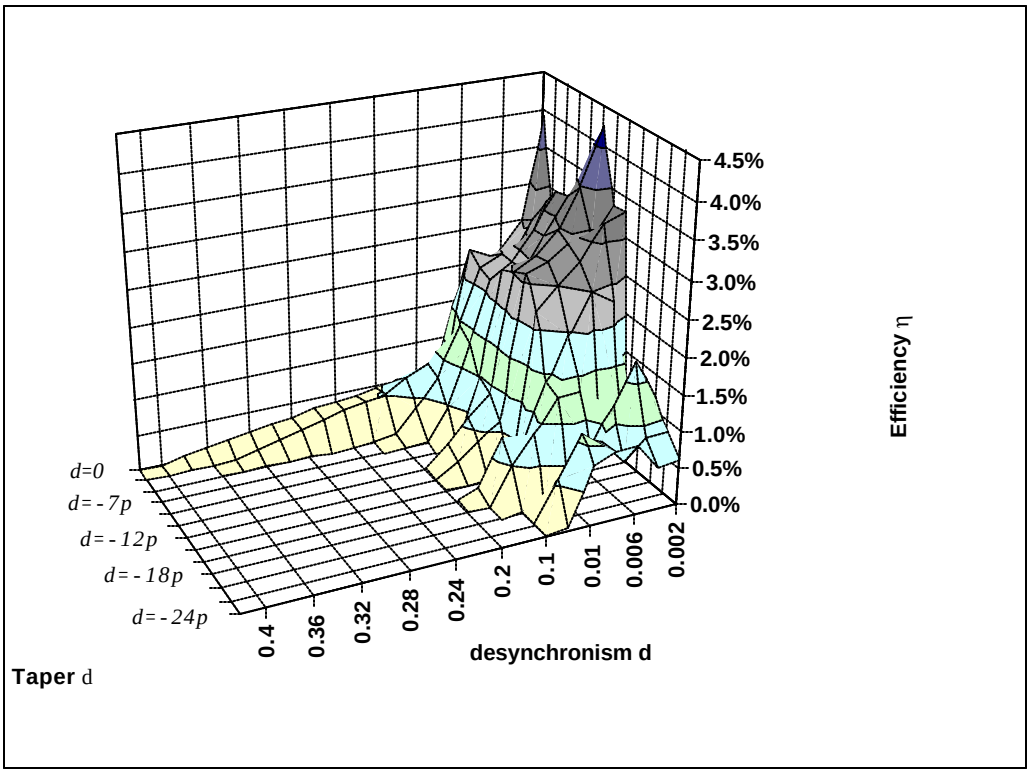

Figure 34. Efficiency $\eta(d,\delta)$ for Negative Taper.

For modest taper rates $d = -6p, -7p, -8p$, the efficiency increases from $h = 2.9\% \rightarrow 3.3\%$. With taper rate of $d = -9p$, maximum efficiency $h = 4.2\%$ is reached at $d = 0.002$. Again sidebands are present and responsible for this enhancement in efficiency. For $d = -14p \rightarrow -20p$ the peak efficiency is shifting slightly from $d = 0.002 \rightarrow 0.004$ and efficiency diminishes from $h = 3.3\% \rightarrow 1.7\%$. Further increase of the taper rate $d \rightarrow -24p$, results in a decrease in efficiency to 1% at slightly larger $d = 0.006$.

Figure 35 shows the width of desynchronism *Dd* where the FEL can operate. Values of *Dd* against the taper rate *d* were plotted.

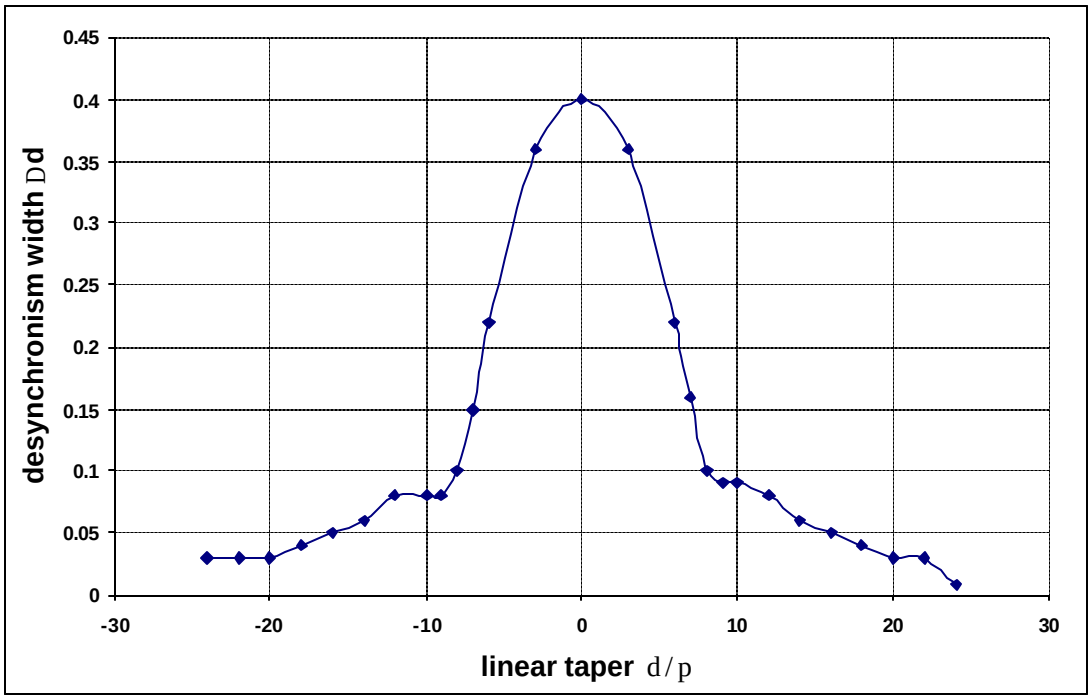

Figure 35. Effective Desynchronism Width.

Note that $Dd(d)$ has the same shape as the gain $G(d)$ curve in Figure 31, with a maximum at $d = 0$ and decreasing rapidly as $|d|$ increases. In the region where $|d| \approx \pm 8p$ the rate of descent becomes much less rapid, indicating that something special happens there.

The change in slope near $d \approx \pm 8p$ is explained by looking at the gain curve (gain versus phase velocityn_0) as δ changes. Figure 36 shows that there are two gain peaks of equal height $d = -8p$. There are also two gain peaks when $d = +8p$, but on the opposite side of resonance $(n = 0)$ where $(v < 0)$. These peaks act together, in either the $d = \pm 8p$ cases, to further amplify the optical field. The transition in plateau at $d = \pm 8p$ results from the FEL switching for one gain peak to a second.

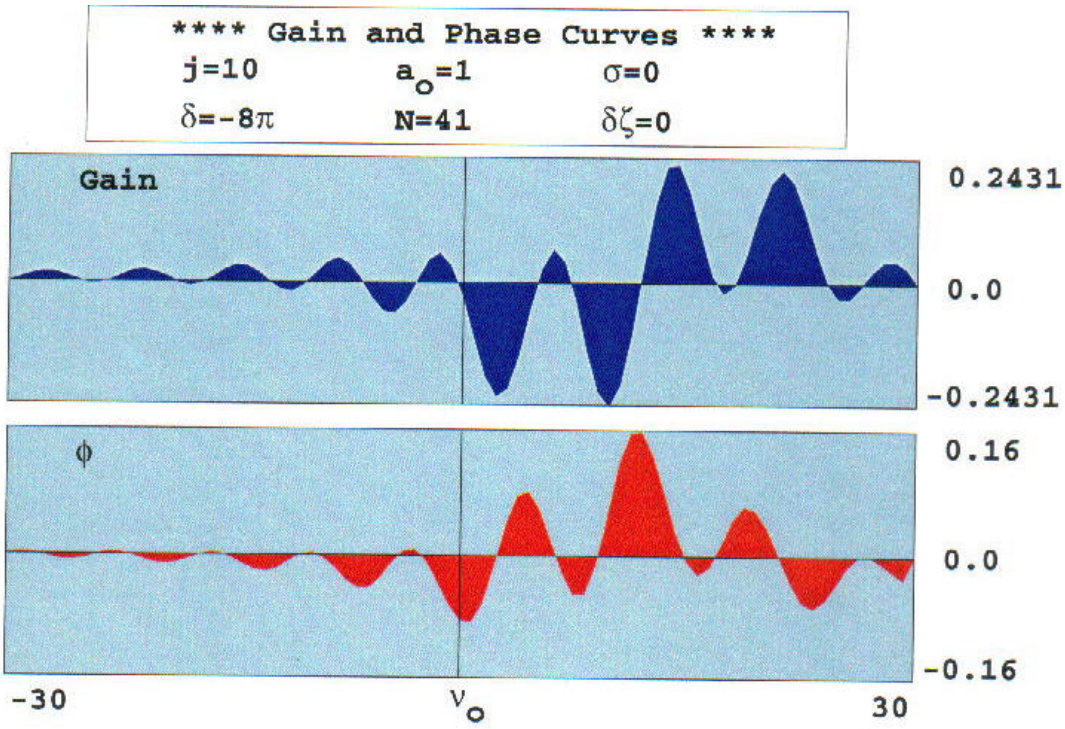

Figure 36. Comparable Peaks in Gain Spectrum, $\delta = -8\pi$.

F. ENERGY SPREAD

The energy spread resulting from the FEL interaction can potentially limit the performance of a high power FEL using energy recovery. Energy recovery is desirable because it can significantly increase the FEL efficiency and reduce the size of beam dump. In the experiment we describe, electron beam recirculation is considered feasible only if the induced energy spread, $\Delta g / g$ is less than 6%. If it is larger, then bending magnets are not able to feed back the beam to the accelerator and the FEL stops operating.

In order to take into account that limiting factor, we measure the width Δn_e from the electron distribution $f(n, n)$ in the FEL pulse evolution simulations. Accordingly we calculate the energy spread using $\Delta g / g = \Delta n_e / 4p N$, where $N = 41$. In Figure 37, the energy spread induced by the FEL interaction is plotted as a function of desynchronism d and positive taper d.

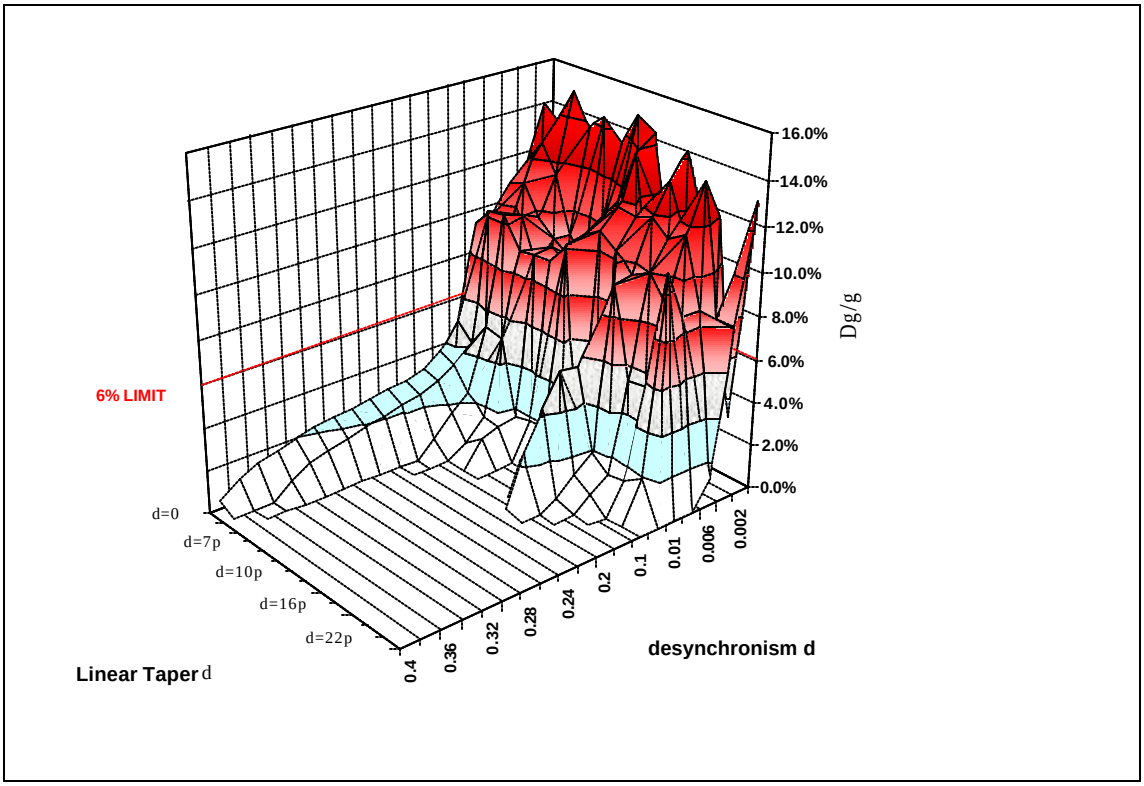

Figure 37. Electron Energy Spread for Positive Taper.

The induced electron beam energy spread for the conventional undulator $(d = 0)$ has a peak energy spread of 14% occurred at $d = 0.002$. The strong fields cause the trapped-particle instability and consequently the energy spread is moved outside the 6% design tolerance. The induced energy spread decreases with increasing the desynchronism, and falls below the desired level at a desynchronism value of $d = 0.04$, and remains below the 6% for all larger values of *d*.

For the positive tapered undulator, the induced energy spread is slightly decreased. For some values of desynchronism $d < 0.05$ and taper $d < 10p$ we are still outside of the limit that imposed for safe recirculation. Unfortunately this is the region in which we have peak efficiency. A further increase in the taper rate $d > 10p$ results a smaller value for *d* for which the energy spread is acceptable. The minimum desynchronism that reduces the energy spread down to the desired 6% is given at the second column of the Table 9.

Figure 38 shows the final induced electron beam energy spread produced by inversely tapered undulators. The energy spread $\Delta\gamma/\gamma$, as a function of desynchronism d and tapering rate d, is plotted.

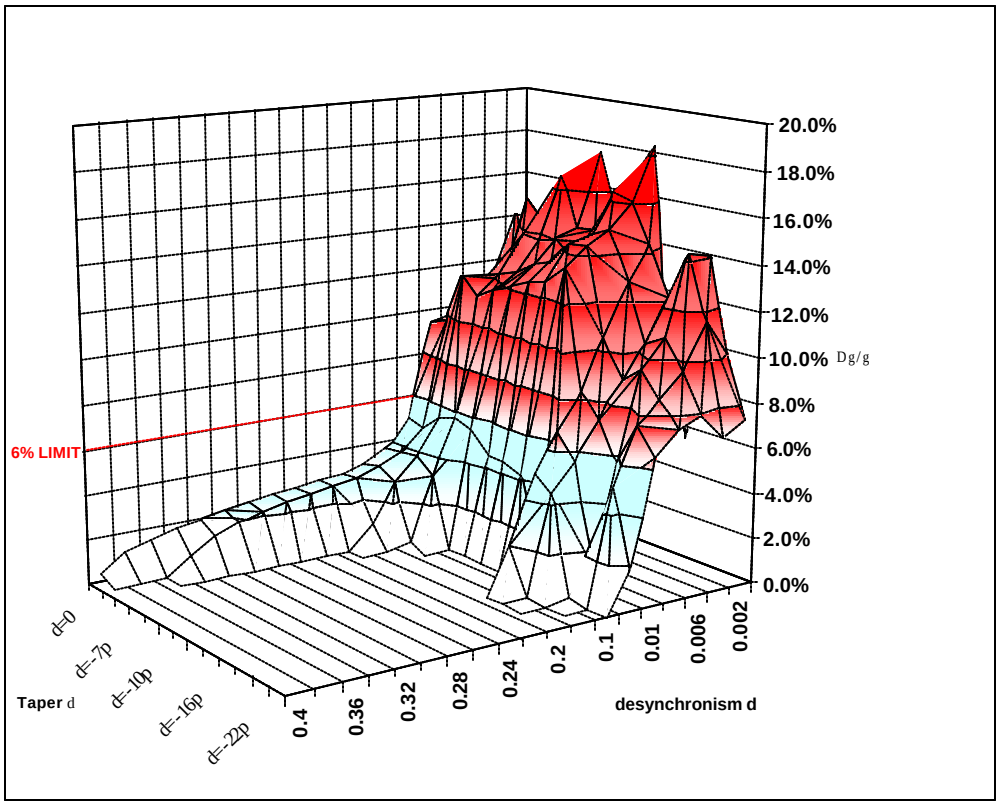

Figure 38. Electron Energy Spread for Negative Taper.

The electron energy spread curves follow the same trend as the power curves. For high power, there is a large energy spread. For taper $d = -9p$ the maximum value is 18% at $d = 0.002$. Recall that for $d = 0$, the maximum value is 14% at $d = 0.002$. After $d = 0.05$ the energy spread drops to less than 6% for all the tapering rates and there is no constraint to the FEL operation. The inverse tapered undulator does not appear to be desirable for recirculating the electron beam. This is the trade-off of the enhancement in the efficiency with the inverse taper. The minimum desynchronism for which the energy spread constraint is not met for the inverse tapered undulators is given at the fifth column of the Table 9.

Table 9 is obtained from previous Figures and helps to summarize the values of desynchronism d and taper d, where we have acceptable results that meet the requirements.

- min d for $(\Delta g / g < 6\%,$ acceptable energy spread)
- max d for $h > 0$ (FEL operation)

In this way we are able to determine the operational range of the FEL as a function of d and d.

Positive d	Min d	Max d
0	0.004	0.4
3π	0.05	0.36
6π	0.05	0.22
7π	0.05	0.16
8π	0.05	0.1
9π	0.05	0.09
10π	0.03	0.09
12π	0.01	0.08
14π	0.02	0.06
16π	0.02	0.05
18π	0.01	0.04
20π	0.01	0.03
22π	0.02	0.03
24π	0.006	0.008

Negative d	Min d	Max d
-3π	0.05	0.36
-6π	0.05	0.22
-7π	0.05	0.15
-8π	0.05	0.1
-9π	0.05	0.08
-10π	0.05	0.08
-12π	0.05	0.08
14π	0.05	0.06
-16π	0.03	0.05
-18π	0.02	0.04
-20π	0.01	0.03
-22π	0.02	0.03
-24π	0.02	0.03

Table 9. Desynchronism Values Meeting the Energy Spread Limitation and Efficiency.

G. EXPERIMENTAL AND SIMULATION RESULTS –COMPARISON

In the experiment, tapers were obtained by inserting precision shims at either end of the wiggler. Dial gauges on either side of the wiggler measured the position and gap of the wiggler for each taper value. Since the variation of the wiggler field with gap size is known, the field taper can be calculated from the gap taper [Ref. 40].

Three values of taper, $d = -7p, 0, 10p$ were examined with the following experimental results compared to simulations.

- Efficiency η

	Experiment	Simulations
d=-7π	2.0%	1.54%
d=0	1.5%	1.0%
d=10π	0.62%	0.67%

- Energy Spread Δγ/γ

	Experiment	Simulations
d=-7π	2.3%	3.1%
d=10π	1.6%	1.8%

- Desynchronism Width d

	Experiment	Simulations
d=-7π	0.15	0.10
d=0	0.2	0.35
d=10π	0.075	0.07

Table 10. Experiment and Simulations Results.

We used the value of efficiency that allows safe recirculation. For inverse taper $d = -7p$, we disregard the highest efficiency h =3.2% at d=0.004 because it gives energy spread $\Delta g / g \sim 14\%$, which is almost twice the allowed limit. The same tactic was followed for positive taper and so we did not accept h =1.9% at d=0.002 since $\Delta g / g \sim 15\%$. For the zero taper case, the efficiency was lower than the experiment. The peak efficiency of $h = 3.9\%$, at $d = 0.002$, was accompanied by energy spread $\Delta g / g \sim 14\%$. It is possible to reduce the energy spread by increasing desynchronism d. At $d = 0.02$ the efficiency is $h = 1.54\%$, while the energy spread is $\Delta g / g = 7.5\%$. At $d = 0.03$ the energy spread is

$\Delta g/g = 5.7\%$ with $h = 1.32\%$. For all the above cases, safe recirculation near $\Delta g/g \sim 6\%$ was the goal. The FEL interaction worked well above the engineering design for the specific experiment.

For the energy spread $\Delta g/g = \Delta n/4p\,N$ we used Δn from simulations, when the desynchronism d was at the upper limit and the efficiency was marginal. In that region the optical and the electron pulse fail to overlap and power was reduced to zero. For the inverse taper $d = -7p$ that happened at $d = 0.1$, where the efficiency was $h = 0.47\%$ and for positive taper $d = 10p$ that condition was met at $d = 0.05$ with $h = 0.6\%$.

H. CONCLUSIONS

For small values of taper and with small values of d, the FEL exhibits the trapped-particle instability. Increasing either desynchronism d or taper rate d the FEL easily moves to a more stable regime, even though the efficiency is lower. This stability is needed in some applications, where the absence of side bands is crucial. For example, the use of the FEL in human surgery requires a narrow energy spectrum in order to achieve the exact desirable wavelength ($l = 6.45\,\mu$m) [Ref. 41].

Negative taper produces better extraction efficiency than positive taper as theoretical studies by Saldin, Schneidmiller and Yurkov have shown [Ref. 37]. Unfortunately this is not accompanied by reduction in the energy spread as h is directly related to $\Delta g/g$, recall $h = <\Delta g\,mc^2>/g\,mc^2$. At $d = -9p$, we have a 0.3% increase from zero taper, which results $h = 4.2\%$. In this manner, we not only enhance the efficiency, but move away from the trapped-particle instability region.

When the FEL is operated with higher $Q = 50$, the gain per pass is significantly more than the loss per pass. One result was that the range of desynchronism values when the FEL operates with a gain above threshold increased compared to the lower Q case. Figure 39 shows the desychronism curve width Δd plotted against the positive and negative taper rate d. The superimposed $G(d)$ shows the clear correspondence between increased gain G and increased desychronism curve width Δd.

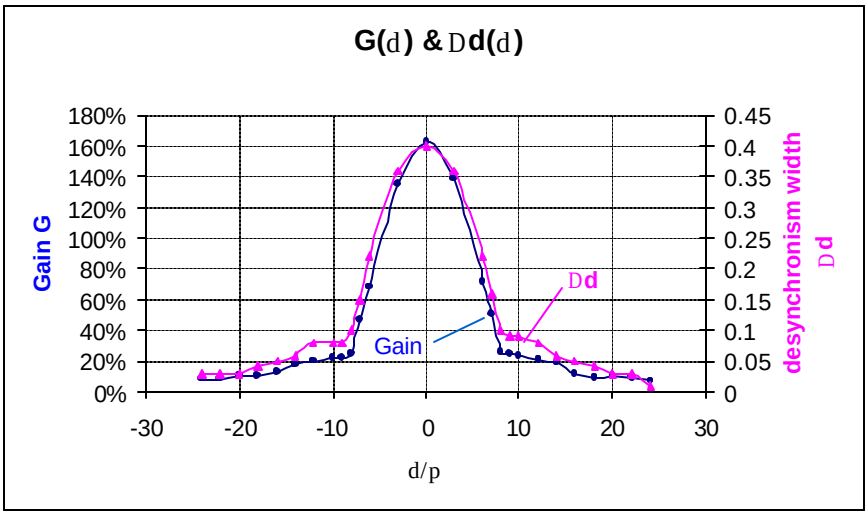

Figure 39. Gain G(δ) and Desynchronism Width Δd(δ).

The maximum gain occurs with no tapering, $d = 0$, as would be expected. As the taper rate d increases or decreases, the gain decreases from 160% to about 40% symmetrically around $d = 0$. At positive or negative taper rates of about $d = \pm 8p$, the gain plateaus decrease much more slowly with the increasing taper rate. While the taper rate increases in magnitude from $|d| = 8p$ out to $|d| = 24p$, the gain decreases from about 40% down to about 10%.

The gain plateau at large values of taper begins at a value of taper d that causes the gain spectrum to change shape so that there are two peaks with nearly the same peak gain. As the taper is increased and the peak available gain decreases, the gain spectrum acquires multiple peaks with comparable gain. As the primary gain peak decreases other surrounding gain peaks increase in comparison. As the peak available gain increases, or decreases, at any value of tapering, the desynchronism curve width Δd increases or decreases correspondingly. With more gain available there are more values of desynchronism that are above the threshold making the desynchronism curve wider.

The simulations and the experimental data are in good agreement with analytic theory. Theory indicates that as taper increases, the desynchronism width decreases. The experiment shows this trend, but not as clearly as the simulation data. There is only one significant deviation between simulation and experimental results. The desynchronism

width for zero taper is $D d = 0.35,$ compared to $\Delta d = 0.2$ in the experiment. The disagreement has led to reconsideration of the experimental procedure for this data point [Ref. 41].

The wiggler design can be important in the energy recovery FELs. The specific IR TJNAF FEL demo was designed to operate in the safe mode where $\Delta g / g < 6\%$, even if it were capable of higher extraction efficiency Current developments at TJNAF make feasible the recirculation of the electron beam for all values of $\Delta g / g$ that we found in the simulations runs.

VI. CONCLUSIONS

The missile defense capabilities currently under development must not only review past wars but more importantly plan for the future. Tactical missile threats still in existence from past wars and their capabilities are rapidly improving with the result that it will be much more difficult to counter such threats in the future. The current development of weapons is centered on shortsighted decisions based on current threats and technical challenges. By the time some weapons are deployed they are outdated and ineffective. Light-based weapons offer the solution to this problem since they possess layered capability to counter a potential threat.

FEL defensive capability prompted the U.S. Congress to approve a $15 million grant to the Thomas Jefferson National Accelerator Facility. At present, the TJNAF FEL is the most powerful FEL in the world and operates at more than 2 kW average power for many hours at a time. One transitional step for the l MW output power, required for a weapon, is the proposed l00 kW upgrade. Multimode simulations used at NPS show that this development is feasible.

For the TJNAF 100kW FEL parameters, the inverse taper undulator of $\Delta = -p$ achieved the highest final power at a desynchronism of $d = 0.04$ for $Q = 4.2$. The output power produced was $P \sim 120$ kW, which is above the 100 kW objective. The small values of the induced electron energy spread (~3.5%) made it possible to explore a design with 10% losses ($Q = 10$) in an optical cavity. The higher Q factor was chosen to increase the efficiency of the system, while maintaining the induced energy spread well below the 15% engineering limit. The results related with the $Q = 10$ design were

- the inverse step-taper undulator $\Delta = -p$ achieved the highest final power $P = 190$ kW at a desynchronism of $d = 0.01$.
- The inverse linear taper $d = -2p$ achieved the highest final power $P = 200$ kW at a desynchronism $d = 0.01$.

The validity of our results have been compared to experiments conducted at the TJNAF FEL facility. Various taper rates and desynchronism values were studied. The purpose of the simulations was to compare experiments with theory, and, by using a

wider range of parameters than allowed in the experiment, to extract more physical meaning from the results. The simulations and the experimental data were consistent with analytic theory. Theory indicates that as a taper increases, the desynchronism width decreases. The experiment shows this trend, but not as clearly as the simulation data. There is only one significant discrepancy between simulation and experimental results, that has resulted in ongoing discussion about the validity of the experimental observation in this case.

Thus it is possible to conclude that FELs have the potential to be developed into a compact, reliable and efficient weapon. This development leads not only to a new military era but opens the door for commercial and scientific applications. The extremely high industrial and technological momentum that exists makes FEL development feasible with high level pay-offs.

LIST OF REFERENCES

[1] Jane's on Line, TRW Nautilus Programme/Tactical High Energy Laser (THEL) Programme, 11 July 2001.

[2] JED, November 2000, VOL.23,No.11.

[3] Hecht, The Laser Guidebook, 1986.

[4] Patrick O'Shea and Henry P. Freund, Free-Electron Lasers: Status and Applications, Science Vol. 292, 8 June 2001.

[5] Madey, J. J., Applied Physics. 42, 1971.

[6] Hecht, Optics, Third edition, 1998.

[7] R. D. McGinnis, Free Electron Development for Directed Energy, Dissertation, Naval Postgraduate School, December 2000.

[8] Dan Leslie, Trex, e-mail, May 17,2001.

[9] Eric J. Anderson, "Total Ship Integration of Free Electron Laser", Master's Thesis, Naval Postgraduate School, September 1996.

[10] Lt. Gen. Lester L. Lyles, Missile Defense Still Important, August 5, 1997.

[11] W. B. Colson, A. Todd, G. R. Neil, A High Power FEL using a Short Rayleigh Length, Nucl. Instr. and Meth. ? xxx (2002) xxx.

[12] Free Electron Laser Development for Naval Applications Workshop, Working Group C Summary, Virginia, June 2001.

[13] J. W. Goodman, Introduction to Fourier Optics, 1996.

[14] http://hyperphysics.phy-astr.gsu.edu/hbase/atmos/blusky.html

[15] Robert D. Stock, MIT Lincoln Lab, June 2001.

[16] A. Todd, NPS Presentation, May 23,2001.

[17] R. A. Lyon, Prime Power for Shipboard High-Average Power FELs, Master's Thesis, Naval Postgraduate School, December 1994.

[18] Free Electron Laser Development for Naval Applications Workshop, Working Group A summary, Virginia, June 2001.

[19] G. R. Neil, private e-mail, May, 2001.

[20] C. A. Primmerman, Free Electron Laser Development for Naval Applications Workshop, Virginia, June 2001.

[21] Free Electron Laser Development for Naval Applications Workshop, Working Group C Summary, Virginia, June 2001.

[22] Defense Science Board Task Force on HEL, June 2001.

[23] Planning Study for Advanced National Synchrotron–Radiation, March 1984.

[24] W. B. Colson, Fundamental FEL Theory and New Principles for Advanced Devices, 1988.

[25] W. B. Colson, C. Pellegrini, ?. Renieri (Eds.), Laser Handbook, Vol. 6, North-Holland, Amsterdam, (Chapter 5), 1990.

[26] W. B. Colson, Short Wavelength FELs in 2000.

[27] W. T. Silfvast, Laser Fundamentals, 1996.

[28] W. B. Colson. PH 4055 in class notes, Jan. 2000.

[29] S. Benson, et., al., Nucl. Instr. And Meth.,1999.

[30] http://www.tjnaf.org

[31] L. Merminga, RF Stability in Energy Recovering FELs: Theory and Experiment. Nucl. Instr. and Meth. ? xxx (2001) xxx.

[32] G. R. Neil e-mail, May 2001.

[33] ? . ? . Kroll, ?. ?. Morton, ? . ?. Rosenbluth, Phys. Quantum Electron. 7 (1980) 89.

[34] D. A. Jaroszynski, R. Prazeres, F. Glotin, J. M. Ortega, Nucl. Instr. and Meth. ? 358 (1995) 224.

[35] D. A. Jaroszynski, R. Prazeres, F. Glotin, J. M. Ortega, D. Oepts, A. F. G. van der Meer, G. Knippels, P. W. van Amersfoort, Nucl. Instr. and Meth. ? 358 (1995) 228.

[36] D. A. Jaroszynski, R. Prazeres, F. Glotin, O. Marcouille, J. M. Ortega, D. Oepts, A. F. G. van der Meer, G. Knippels, P. W. van Amersfoort, Nucl. Instr. and Meth. ? 375 (1996) 647.

[37] E. L. Saldin, ?. ?. Schneidmiller, ? . V. Yurkov, Nucl. Instr. and Meth. ? 375 (1996) 336.

[38] Benson, S., Gubeli, J., and Neil, G. R., "An Experimental Study of an FEL Oscillator with a Linear Taper", TJNAF, Newport News, VA, 2000.

[39] W. B. Colson, Fundamental FEL Theory and New Principles for Advanced Devices, Proc. SPIE 738, 2-27 (1988).

[40] A. Christodoulou, D. Lampiris, W. B. Colson, P.P. Crooker, J. Blau, R. D. McGinnis, S. V. Benson, J. F. Gubeli, G. R. Neil, Nucl. Instr. and Meth. ? xxx (2001) xxx.

[41] Vanderbilt University, Human Surgery using Free Electron Laser (2000).

[42] W. B. Colson, Private Communication, December 2001.

THIS PAGE INTENTIONALLY LEFT BLANK

INITIAL DISTRIBUTION LIST

1. Defense Technical Information Center
   Ft. Belvoir, Virginia

2. Dudley Knox Library
   Naval Postgraduate School
   Monterey, California

3. Professor William B. Colson, Code PH/Cw
   Department of Physics
   Monterey, California

4. Professor Robert L.Armstead, Code PH/Ar
   Department of Physics
   Monterey, California

5. Chairman, Physics Department
   Naval Postgraduate School
   Monterey, California

6. Professor Peter Crooker,
   Department of Physics and Astronomy
   Honolulu, HI

7. Maj. Konstantinos Polykandriotis
   Athens, Greece

8. Engineering & Technology Curricular Office (Code 34)
   Naval Postgraduate School
   Monterey, California